

---

# Physics-constrained symbolic model discovery for polyconvex incompressible hyperelastic materials

Bahador Bahmani · WaiChing Sun

Received: October 9, 2023/ Accepted: date

**Abstract** We present a machine learning framework capable of consistently inferring mathematical expressions of the hyperelastic energy functionals for incompressible materials from sparse experimental data and physical laws. To achieve this goal, we propose a polyconvex neural additive model (PNAM) that enables us to express the hyperelasticity model in a learnable feature space while enforcing polyconvexity. An upshot of this feature space obtained via PNAM is that (1) it is spanned by a set univariate basis that can be re-parametrized with a more complex mathematical form, and (2) the resultant elasticity model is guaranteed to fulfill the polyconvexity, which ensures that the acoustic tensor remains elliptic for any deformation. To further improve the interpretability, we use genetic programming to convert each univariate basis into a compact mathematical expression. The resultant multi-variable mathematical models obtained from this proposed framework are not only more interpretable but are also proven to fulfill physical laws. By controlling the compactness of the learned symbolic form, the machine learning-generated mathematical model also requires fewer arithmetic operations than the deep neural network counterparts during deployment. This latter attribute is crucial for scaling large-scale simulations where the constitutive responses of every integration point must be updated within each incremental time step. We compare our proposed model discovery framework against other state-of-the-art alternatives to assess the robustness and efficiency of the training algorithms and examine the trade-off between interpretability, accuracy, and precision of the learned symbolic hyperelasticity models obtained from different approaches. Our numerical results suggest that our approach extrapolates well outside the training data regime due to the precise incorporation of physics-based knowledge.

**Keywords** Interpretable model, hyperelasticity, symbolic regression, polyconvex neural additive Model

## 1 Introduction

Engineering analysis and computer simulations of solid behaviors often involve solvers that predict admissible solutions that fulfill a set of constraints. As explained in [Kirchdoerfer and Ortiz \[2016\]](#), these constraints can be (1) the balance principles, which are often regarded as ground truth, and (2) the constitutive laws, of which the legitimacy of employing such supplement constraints depend on the specific situation upon which the model is used [[Boyce and Arruda, 2000](#)]. For instance, while vehicle crash simulations for safety analysis [[Le Guennec et al., 2018](#), [Barbani et al., 2014](#)] and those for computer animation and gaming [[Grinspun et al., 2003](#)] can both benefit from improving high fidelity, the demands on robustness, accuracy, efficiency, and risk tolerance on predictions are significantly different for these two applications. This difference often leads to different modeling choices, ranging from simplified models that offer speed and robustness, often at the expense of accuracy, to highly sophisticated models or multiscale constitutive

---

Corresponding author: WaiChing Sun

Associate Professor, Department of Civil Engineering and Engineering Mechanics, Columbia University, 614 SW Mudd, Mail Code: 4709, New York, NY 10027 Tel.: 212-854-3143, Fax: 212-854-6267, E-mail: wsun@columbia.edu

updates from representative elementary volumes that exhibit higher fidelity, precision, and accuracy even at the expense of efficiency [Dafalias, 1984].

For soft materials that remain elastic while undergoing large isochoric deformation, modeling frameworks, such as hypoelasticity (cf. Truesdell [1955], Green [1956], Freed et al. [2010]) and hyperelasticity (cf. Ogden [1997], Holzapfel et al. [2000], Mihai et al. [2017], Mooney [1940], Rivlin and Saunders [1951]) are some of the more popular choices for these different applications. In the former framework, one may see to directly establish a relationship between a pair of stress and strain measures. For instance, one may compose an isotropic function that maps the left Cauchy-Green tensor  $\mathbf{b}$  to Cauchy stress for isotropic elastic materials [Truesdell, 1955]. Hyperelasticity models, on the other hand, provide an alternative strategy where one considers that the deformation increases Helmholtz free energy, and the stress and its corresponding tangent stiffness are the Jacobian and the Hessian of this free energy with respect to the deformation measure. This latter approach provides a convenient and flexible way to fulfill thermodynamics consistency, enforce different symmetries, and, if desired, ensure the stability of the material models by enforcing properties (e.g., growing condition, convexity, polyconvexity) on the elastic energy functions. As such, prior knowledge of the material behaviors, such as the lattice structure of a crystal (for symmetries) and the shape memory effect of certain alloys (for multiple potential wells), can be easily incorporated into the modeling process. If this prior knowledge can be incorporated by deducing specific *form* of the energy functional, then the last remaining task to complete the model is to find the actual *parametrization* of the model that fulfill all the constraints of both the experimental data and prior knowledge of physics.

In addition to hand-crafting the mathematical expression, a variety of alternatives, such as artificial neural network [Vlassis et al., 2020, Liu et al., 2020, Thakolkaran et al., 2022, Klein et al., 2022, Tac et al., 2022], Gaussian process [Frankel et al., 2020, Fuhs and Bouklas, 2022], and symbolic regression [Abdusalamov et al., 2023], are often used to generate the closure of the constitutive laws. In the former case, the feedforward neural network may provide the expressibility (the ability to fit any complex data) necessary to yield precise models [Hornik et al., 1989, Hsu et al., 2021]. However, underfitting, overfitting, the lack of interpretability, and the incompatibility of physics constraints could all negatively impact the quality of the learned models. While the underfitting/overfitting issue can be circumvented with hyperparameter tuning, both the lack of interpretability and the incompatibility with known physics constraints are issues that make the resultant models not feasible for the intended engineering applications, especially for high-consequent applications such as patient-specific simulations or design of structural components for civil infrastructure. For example, Shen et al. [2004] and Liang and Chandrashekhara [2008] proposed training a hyperelasticity energy functional for elastomeric foams. Liang and Chandrashekhara [2008] used strain invariants as inputs for the neural network and conducted training based on the calculated stress as labeled data for supervised learning. Meanwhile, Le et al. [2015] introduces the neural network hyperelasticity models to upscale constitutive responses for representative elementary volume, where energy, stress, and tangents are obtained from the neural network. There has been a rapidly growing body of work on hyperelasticity model parametrized by neural networks trained by Sobolev norm [Vlassis et al., 2020, Vlassis and Sun, 2021, Vlassis et al., 2022], neural ordinary differential equation [Tac et al., 2022] as well as multi-objective optimization problem that attempts to fulfill all data and physics constraints [Klein et al., 2022, Fernández et al., 2022].

This paper aims to formulate a feasible machine learning framework that can consistently generate hyperelasticity models whose properties can be easily interpreted and fulfill all the known physical constraints. A critical technical barrier we would like to overcome is the difficulty of determining the expression tree in the symbolic regression that simultaneously satisfies the polyconvexity of the learned model. While there have been works on generating polyconvex neural network models via neural networks, to the author's best knowledge, this contribution is the first attempt to develop a machine learning algorithm to generate a polyconvex hyperelasticity model expressed via mathematical expression. To achieve this objective, we use a parameterization strategy similar to the neural additive model [Agarwal et al., 2021] and the recently proposed quadratic extension [Bahmani et al., 2023] of which a feature space spanned by univariate functions obtained from neural networks, while improving the machine learning algorithm by introducing physical constraints and polyconvexity to ensure the desirable properties of the learned hyperelastic models. To improve interpretability without comprising expressivity and accuracy, we introduce an additional step where we use symbolic regression on the feature space such that it can be approximated by basis function expressed analytically. As the polyconvexity can be guaranteed by energy functional written

in the specific additive form (cf. [Hartmann and Neff, 2003]), this feature enables us to express the resultant hyperelasticity model as a function of the features of the strain invariants that exhibits polyconvexity.

### 1.1 Reviews on Physical Constraints for Elasticity Models

Previous machine learning models have been trained with prior physics knowledge incorporated as constraints (e.g., [Teichert et al., 2019, Liu et al., 2020, Masi et al., 2021, Tac et al., 2022, Vlassis et al., 2022]). The basic strategy is similar to those used in physics-informed neural network paradigms considered seminal by many for solving partial differential equations where a variety of loss functions are employed to ensure that the learned solution satisfied the physical constraints [Raissi et al., 2019, Lagaris et al., 1998]. However, as the training is designed to minimize, not eliminate, the discrepancies, there is a possibility of violating these constraints when dealing with data not used during training, especially in the extrapolation regime [Bronstein et al., 2021]. Furthermore, enforcing multiple constraints into the loss function may lead to a multi-objective optimization problem where gradient conflicts among different objectives may further complicate the search for the global optima [Yu et al., 2020, Bahmani and Sun, 2021], which is already an NP-hard problem [Jin et al., 2016].

To address these challenges, several neural network architectures have explicitly incorporated all or subsets of physics laws by design for constitutive modeling [Heider et al., 2020, Xu et al., 2021, Linka et al., 2021, Tac et al., 2022, As'ad et al., 2022, Chen and Guilleminot, 2022, Cai et al., 2023]. The by-design strategy can be selecting the optimal parameterization of input variables (e.g., using strain invariants instead of the strain tensor for isotropic materials) or modifying neural network architecture to preserve symmetry, invariance, and equivariance. By fulfilling the proposed physical constraints by design, the learned models that inherently fulfill the physical constraints are more robust, especially in the data-limited regime. In fact, this is in line with the history of hand-crafted hyperelasticity models in which material symmetry has already been heavily leveraged to yield a specific form of mathematical expression that reduce the number of independent variables, enforce symmetry and thermodynamics constraints [Ogden, 1997, Schröder and Neff, 2003, Holzapfel et al., 2000] and induce desirable properties, such as polyconvexity [Hartmann and Neff, 2003] and quasi-convexity [Ball, 1987, Shirani and Steigmann, 2022]. In this paper, we will adopt this latter by-design strategy while leveraging the power of the neural additive model and symbolic regression to improve further the model obtained from the machine learning algorithm.

### 1.2 Reviews on Interpretability Machine Learning Constitutive Laws

The learnable parameters, such as weights and biases, parametrize the learned function obtained from training neural networks. As such, the current trend of increasingly deep and large neural networks often leads to significant challenges in interpreting and examining the *global* property of the machine learning models [Dayhoff and DeLeo, 2001, Oh et al., 2019]. For instance, while it is possible to use a sampling technique to test the robustness of the learned model for a set of strain inputs against constraints, satisfying the physical constraints for a subset of data points only estimates the population loss. This accuracy shown in the sampling test is only a necessary but not sufficient condition for the model accuracy in general.

An obvious strategy to circumvent this issue is to derive alternative parameterization that (1) may lead to more compact mathematical expression where analyses (such as calculating the acoustic wave speed and detecting the loss of ellipticity) typically performed on hand-craft models can be conducted. In contrast to ANN-based methods, symbolic regression (SR) methods are free-form approaches where the equation form is discovered in a data-driven manner using gradient-free methods like genetic algorithms. The application of SR algorithms in data-driven mechanics has proven effective in discovering plasticity yield functions [Versino et al., 2017, Bomarito et al., 2021, Park and Cho, 2021]. While initial attempts do not enforce physics knowledge, data augmentation via physics intuitions has shown improvements in SR performance Versino et al. [2017]. In a recent work by Abdusalamov et al. [2023], an SR method for discovering hyperelastic materials is introduced, directly utilizing energy functionals. This approach offers advantages in terms of thermodynamics consistency. However, it can be computationally expensive due to the requirement for symbolic gradient calculations during optimization iterations.

The advantage of SR machine learning methods is their ability to provide explicit equation forms, which are often simpler than neural network operations. However, various challenges have hindered their popularity compared to ANN-based methods in mechanics. Firstly, their lack of scalability, especially in multidimensional data settings, is attributed to the combinatorial nature of their search space. Secondly, incorporating mechanistic constraints, especially those related to gradient operations like ellipticity, is not a straightforward task in these algorithms. This difficulty arises from their use of gradient-free optimizers and the costly process of symbolic gradient calculation, in contrast to the efficiency of automatic differentiation methods used in ANN-based methods. Sparse regression within a predefined library of modes [Brunton et al. \[2016\]](#) offers a potential method to bridge the gap between scalability and interpretability in model identification. [\[Flaschel et al., 2021, Wang et al., 2021\]](#) develop a material discovery formulation from a predefined library of material models. Their approach indirectly discovers a material model from displacement and force data over the boundary of the material sample. Similarly, [Linka and Kuhl \[2023\]](#) employs a library of modes inspired by classical constitutive models and prior physics knowledge to directly learn energy functionals from strain and stress data. Each mode’s contribution to the final prediction is trained using a gradient-based optimizer with automatic differentiation as the backbone algorithm. Such predefined modes may introduce significant bias in the modeling and might restrict the learning of complex modes not present in the library. [Wang et al. \[2022\]](#) parameterize the stress tensor as a polynomial function of the strain tensor. However, since the physics constraints, such as material symmetry and thermodynamics constraints, are not explicitly enforced in the formulation, the model is not guaranteed to be compatible with these constraints.

**Remark 1 Alternatives approaches for elasticity problems** The model-free or distance minimization method [\[Nguyen and Keip, 2018, Platzer et al., 2021\]](#) is extended to finite deformation, eliminating the need for any model assumptions. Another model-free approach known as What-You-Prescribe-Is-What-You-Get (WYPIWYG) [Crespo et al. \[2017\]](#) is also employed. Following the WYPIWYG idea, methods based on spline shape functions are also introduced [\[Amores et al., 2019, Moreno et al., 2020, Akbari et al., 2022\]](#). Some research formulates the learning of the constitutive law as a manifold learning problem, searching for the response surface rather than using conventional surrogate models for input-to-output mapping [\[Ibanez et al., 2018, He et al., 2021, González et al., 2020, Bahmani and Sun, 2022, 2023\]](#).

### 1.3 Notation and Organization of the Remaining Paper

The remaining content of this paper is organized as follows. In Section 2, we review the crucial elements needed to construct our model structure, adhering to physics knowledge and mechanical properties of incompressible hyperelastic materials. These properties include isotropy, material objectivity, polyconvexity, and coercivity. Our model discovery method is outlined in Section 3, where we summarize our two-step approach. We then describe the specific structure of the neural network and symbolic regression algorithms used to ensure polyconvexity of the final discovered energy functional. In Section 4, we provide reduced forms of the proposed formulation to handle common experimental setups, which will be useful for calibrating the model from experimental data. To demonstrate the effectiveness of our framework, we find two symbolic models for real and synthetic data in Section 5. Additionally, we provide a discussion on the formal analysis of the discovered models in Section 6.

As for notations and symbols, bold-faced and blackboard bold-faced letters denote tensors (including vectors which are rank-one tensors); the symbol ‘ $\cdot$ ’ denotes a single contraction of adjacent indices of two tensors (e.g.,  $\mathbf{a} \cdot \mathbf{b} = a_i b_i$  or  $\mathbf{c} \cdot \mathbf{d} = c_{ij} d_{jk}$ ); the symbol ‘ $\cdot\cdot$ ’ denotes a double contraction of adjacent indices of tensor of rank two or higher (e.g.,  $\mathbf{C} : \boldsymbol{\varepsilon} = C_{ijkl} \varepsilon_{kl}$ ); the symbol ‘ $\otimes$ ’ denotes a juxtaposition of two vectors (e.g.,  $\mathbf{a} \otimes \mathbf{b} = a_i b_j$ ) or two symmetric second-order tensors [e.g.,  $(\boldsymbol{\alpha} \otimes \boldsymbol{\beta})_{ijkl} = \alpha_{ij} \beta_{kl}$ ]. We also define identity tensors:  $\mathbf{I} = \delta_{ij}$  and  $\mathbf{II} = (\delta_{ik} \delta_{jl} + \delta_{il} \delta_{jk})/2$ , where  $\delta_{ij}$  is the Kronecker delta. As for sign conventions, unless specified, tensile stress and dilative pressure are considered positive.

## 2 Hyperelasticity Formulation: Physics Constraints

In this section, we establish the theoretical foundation upon which we construct our modeling structure, ensuring the incorporation of physics knowledge in the model. First, we delve into the kinematics of finite strain elasticity. Next, we review essential conditions for incorporating physically or empirically inspired constraints, such as polyconvexity. Finally, we derive the most general form of the energy functional, introducing unknown functions that will be parametrized by appropriate hypothesis classes in the following section.

### 2.1 Kinematics of Finite Deformation

For completeness, we briefly review the kinematics of a continuum, which is the input of a path-independent elastic energy functional. Recall that the motion of a material point at the reference configuration  $X \in \Omega_0$  can be describe by the vector field  $\phi(\mathbf{X}) : \mathbb{R}^3 \rightarrow \mathbb{R}^3$  which moves points  $\mathbf{X} = X_I \mathbf{E}_I$  in the reference configuration  $\Omega_0$  to locations  $\mathbf{x} = x_i \mathbf{e}_i$  in the current configuration  $\Omega$ . The deformation gradient tensor  $\mathbf{F}$ , the primary measure of deformation, is the tangent operator of the motion  $\phi$ , i.e.,

$$\mathbf{F} = \nabla^{\mathbf{X}} \phi; \quad F_{ij} = \frac{\partial \phi_i}{\partial X_j}. \quad (1)$$

The stretch vector  $\lambda^N$  along the direction of the unit vector  $\mathbf{N}$  at  $\mathbf{X} \in \Omega_0$  is defined as,

$$\lambda^N = \mathbf{F}\mathbf{N}; \quad \lambda_i^N = F_{ij}N_j. \quad (2)$$

For practical reasons, one may prefer to use the right Cauchy-Green tensor  $\mathbf{C}$  as a deformation measure,

$$\mathbf{C} = \mathbf{F}^T \mathbf{F}; \quad C_{IJ} = F_{iI} F_{iJ}. \quad (3)$$

The right Cauchy-Green tensor is symmetric and positive-definite which is more favorable for numerical calculations. Moreover, it is fully described with respect to the reference coordinate system which may ease analytical derivations by avoiding conversion between spatial and material coordinate systems. The first three principal invariants of the right Cauchy-Green tensor is calculated as follows,

$$I_1 = \text{tr}(\mathbf{C}) = C_{II}, \quad (4)$$

$$I_2 = \text{tr}(\text{adj}(\mathbf{C})) = \frac{1}{2} (I_1^2 - \text{tr}(\mathbf{C}^2)) = \frac{1}{2} (C_{II}C_{JJ} - C_{IJ}C_{IJ}), \quad (5)$$

$$I_3 = \det(\mathbf{C}) = J^2, \quad (6)$$

where  $J$  is the Jacobian of the deformation gradient, i.e.,  $J = \det(\mathbf{F})$  and  $\text{tr}(\cdot)$  and  $\det(\cdot)$  are trace and determinant operators, respectively. In this relation, adjugate operator is defined as  $\text{adj}(\mathbf{C}) = \text{cof}(\mathbf{C})^T = \det(\mathbf{C})\mathbf{C}^{-1}$  where  $\text{cof}(\cdot)$  is the cofactors operator. The importance of the tensor representation based on its invariants will be clarified later. For isotropic hyperelastic materials, the three invariants are sufficient to predict the elastic stored energy and the corresponding stress measure due to coaxiality.

### 2.2 Hyperelasticity Theory of Isotropic Elastic Materials

Presumably, one may, for instance, develop constitutive theories by establishing relations between the deformation gradient and the first Piola–Kirchhoff stress  $\mathbf{P}(\mathbf{F})$ . However, caution must be exercised to avoid violating physics principles such as thermodynamic consistency [Truesdell et al., 2004]. Here, our focus is on the modeling of Green-elastic (hyperelastic) materials that postulate the existence of Helmholtz free energy.

### 2.2.1 Thermodynamic consistency for Green-elastic materials

Assuming that a material produces no entropy locally [Truesdell, 1992], then the material is perfectly elastic. In this case, the second law of thermodynamics, which requires non-negative internal dissipation, is fulfilled by the existence of the Helmholtz free energy, i.e.,

$$\mathcal{D} = \mathbf{P} : \dot{\mathbf{F}} - \dot{W}(\mathbf{F}) = \mathbf{P} : \dot{\mathbf{F}} - \frac{\partial W(\mathbf{F})}{\partial \mathbf{F}} : \dot{\mathbf{F}} \geq 0, \quad (7)$$

where  $W$  is the Helmholtz free energy, and by definition, as the dissipation is always zero for perfect elastic materials, we have,

$$\mathbf{P} = \frac{\partial W(\mathbf{F})}{\partial \mathbf{F}}. \quad (8)$$

### 2.2.2 Objectivity and frame indifference

The free energy function  $W$  must be invariant with respect to any rigid rotation of the reference coordinate system. This is equivalent to say,

$$W(\mathbf{F}) = W(\mathbf{Q}\mathbf{F}) \quad \forall \mathbf{Q} \in \text{SO}(3), \quad (9)$$

where  $\mathbf{Q}$  is any arbitrary rotation tensor belong to the special orthogonal group  $\text{SO}(3)$ , i.e.  $\mathbf{Q}^T \mathbf{Q} = \mathbf{I}$ . This requirement can be satisfied if one defines the strain energy function solely based on the right Cauchy Green deformation tensor, i.e.,  $\bar{W}(\mathbf{C}) = W(\mathbf{F})$ , which leads to the following relation

$$\exists \bar{W}(\mathbf{C}) \text{ s.t. } \mathbf{P} = \frac{\partial \bar{W}(\mathbf{C})}{\partial \mathbf{F}} = 2\mathbf{F} \frac{\partial \bar{W}(\mathbf{C})}{\partial \mathbf{C}} \implies \text{Frame Indifference.} \quad (10)$$

### 2.2.3 Isotropy Condition

An isotropic material exhibits the same strain-stress response under a symmetry transformation, i.e.,

$$W(\mathbf{F}) = W(\mathbf{F}\mathbf{Q}^T) \quad \forall \mathbf{Q} \in \text{SO}(3). \quad (11)$$

For the free energy written in terms of  $\mathbf{C}$ , the isotropy of the constitutive responses imply that,

$$\bar{W}(\mathbf{C}) = \bar{W}(\mathbf{Q}\mathbf{C}\mathbf{Q}^T) \quad \forall \mathbf{Q} \in \text{SO}(3) \implies \text{Isotropic Material.} \quad (12)$$

From the representation theorem for invariants [Gurtin, 1982, Holzapfel, 2002] one may show that this constraint can be satisfied if the free energy can be expressed as a function of only the principal invariants, i.e.,

$$\exists \psi(I_1(\mathbf{C}), I_2(\mathbf{C}), I_3(\mathbf{C})) \text{ s.t. } \mathbf{S} = 2 \frac{\partial \psi(I_1, I_2, I_3)}{\partial \mathbf{C}} \implies \text{Isotropic Material} \quad (13)$$

$$\frac{\partial \psi(I_1, I_2, I_3)}{\partial \mathbf{C}} = \left( \frac{\partial \psi}{\partial I_1} + I_1 \frac{\partial \psi}{\partial I_2} \right) \mathbf{I} - \frac{\partial \psi}{\partial I_2} \mathbf{C} + I_3 \frac{\partial \psi}{\partial I_3} \mathbf{C}^{-1}, \quad (14)$$

where  $\mathbf{S}$  is the second Piola–Kirchhoff stress and  $\mathbf{P} = \mathbf{F}\mathbf{S}$ .

### 2.2.4 Incompressibility Condition

At the incompressibility limit  $I_3 = J = 1$ , hence there is no need to introduce the third invariant as a variable for the free energy of incompressible materials. However, one may introduce a scalar variable  $p$  (hydrostatic pressure) that serves as a Lagrange multiplier to account for the energy required to maintain the incompressibility constraint. Under this condition, the second Piola–Kirchhoff stress can be obtained from

$$\psi = \psi^{\text{uc}}(I_1, I_2) - \frac{1}{2}pU(I_3) \implies \text{Incompressible \& Isotropic Material} \quad (15)$$

$$\mathbf{S} = 2 \frac{\partial \psi^{\text{uc}}(I_1, I_2)}{\partial \mathbf{C}} - p \frac{\partial U}{\partial \mathbf{C}}, \quad (16)$$

$$\frac{\partial \psi^{\text{uc}}(I_1, I_2)}{\partial \mathbf{C}} = \left( \frac{\partial \psi^{\text{uc}}}{\partial I_1} + I_1 \frac{\partial \psi^{\text{uc}}}{\partial I_2} \right) \mathbf{I} - \frac{\partial \psi^{\text{uc}}}{\partial I_2} \mathbf{C}. \quad (17)$$

In this way,  $U(I_3)$  is the energy contribution to penalize the incompressibility constraint, i.e.,  $|I_3| \rightarrow 1$ . For instance, one may choose  $U(I_3) = I_3 - 1$  with  $\partial U / \partial \mathbf{C} = I_3 \mathbf{C}^{-1}$  [Holzapfel \[2002\]](#).

### 2.2.5 Solution Existence and Uniqueness: Polyconvexity Condition

In this section, we will show that the combination of the convex functions of principal invariants is a subclass of polyconvex functions with respect to the deformation gradient which leads to the existence of the solutions for the boundary value problem.

Let's consider the functional  $I(\mathbf{u})$  defined below,

$$I(\mathbf{u}) = \int_{\Omega_0} W(\nabla^X \mathbf{u}) d\Omega, \quad (18)$$

where  $\mathbf{u}(\mathbf{X}) : \Omega_0 \rightarrow \mathbb{R}^3$  is the displacement vector field defined over the open set  $\Omega_0 \subset \mathbb{R}^3$ . The stationary points of this functional satisfy the equilibrium equations of the nonlinear elasticity for a homogeneous body under zero body forces. However, an arbitrary free energy function may not guarantee existence of the minimizers. Convexity of the free energy with respect to the deformation gradient guarantees the existence and uniqueness [Hill \[1957\]](#). However, the uniqueness of the solution is too restrictive and not physical in the bifurcation scenarios such as buckling. A less restrictive condition is polyconvexity, a sufficient condition for the global existence of the solution [Marsden and Hughes \[1994\]](#).

**Definition 1** Convexity: A function  $f(x) : \mathbb{D} \rightarrow \mathbb{R}$  is called convex with respect to its input argument when  $f(\lambda \mathbf{x} + (1 - \lambda)\mathbf{y}) \leq \lambda f(\mathbf{x}) + (1 - \lambda)f(\mathbf{y})$  for any arbitrary  $\mathbf{x}, \mathbf{y} \in \mathbb{D}$  and  $0 < \lambda < 1$ . The strict convexity condition achieves when the equality part becomes inadmissible. In here,  $\mathbb{D}$  resembles the function domain, i.e.,  $\mathbb{D} = \text{dom}(f)$ , which is, in this paper, a subset of real-valued vectors or tensors of rank two.

**Definition 2** Rank-one convex and ellipticity: The free energy  $W(\mathbf{F}) = \psi(\mathbf{C})$  leads to an elliptic system iff the Legendre-Hadamard or rank-one condition holds [[Ball, 1976, 1980, Kuhl et al., 2006](#)]:

$$(\mathbf{M} \otimes \mathbf{m}) : \frac{\partial^2 W}{\partial \mathbf{F} \partial \mathbf{F}} : (\mathbf{M} \otimes \mathbf{m}) \geq 0 \quad \forall \mathbf{M}, \mathbf{m} \in \mathbb{R}^3, \quad (19)$$

where  $\mathbf{M}$  and  $\mathbf{m}$  are arbitrary vectors in the reference and current coordinate systems, respectively. Ellipticity (strongly elliptic) condition is satisfied if the inequality becomes strictly positive. Rank-one convexity is a sufficient condition for material stability and well-posedness of the boundary value problem. Notice that ellipticity requirement does not necessary result in convexity of the strain energy function, so multiple minimizers can be found.

**Definition 3** Quasiconvexity: Morrey's quasiconvexity condition reads as,

$$\int_D W(\mathbf{F}_0 + \nabla^X \mathbf{v}(\mathbf{x})) d\mathbf{x} \geq |D|W(\mathbf{F}_0), \quad (20)$$

for all bounded open sets  $D \in \mathbb{R}^3$  and all vector fields  $\mathbf{v}(\mathbf{x})$ . Quasiconvexity condition along with certain growth and continuity conditions results in the existence of minimizers [Morrey Jr \[1952\]](#).

**Definition 4** Polyconvexity: free energy  $\psi(\mathbf{F})$  is polyconvex iff it is convex with respect to  $(\mathbf{F}, \text{adj } \mathbf{F}, \det \mathbf{F})$ :

$$\exists \text{ convex } f \text{ s.t. } \psi(\mathbf{F}) = f(\mathbf{F}, \text{adj } \mathbf{F}, \det \mathbf{F}), \quad \forall \mathbf{F} \in \mathbb{R}^{3 \times 3} \iff \text{polyconvex } \psi(\mathbf{F}). \quad (21)$$

Polyconvexity results in quasiconvexity but not necessarily convexity.

Notice that all rank-one convexity, quasiconvexity, and polyconvexity conditions are sufficient conditions for existence of minimizers. However, working with the polyconvexity is more preferable since, compared to the others, it is more straightforward to be applied as it has locality without any dependence on arbitrary objects than the deformation gradients (i.e.,  $\mathbf{m}$  and  $\mathbf{M}$ .) In summary, we have the following sequence of conditions from the most restrictive in the left to the most relax to the right:

$$\boxed{\text{polyconvexity}} \rightarrow \text{quasiconvexity} \rightarrow \text{rank one convexity} \rightarrow \text{existence of minimizers} \quad (22)$$

**Lemma 1** A subclass of polyconvex functions can be constructed by convex function  $f_1(\mathbf{F})$ ,  $f_2(\text{adj } \mathbf{F})$ ,  $f_3(\det \mathbf{F})$  in the additive fashion  $\psi = f_1(\mathbf{F}) + f_2(\text{adj } \mathbf{F}) + f_3(\det \mathbf{F})$ .

*Proof.* For brevity, we refer readers to Schröder and Neff [2003] for details,  $\square$

**Lemma 2** If tensor-valued function  $h(\mathbf{A}) : \mathbb{R}^{3 \times 3} \rightarrow \mathbb{R}$  and scalar-valued function  $g(a) : \mathbb{R} \rightarrow \mathbb{R}$  are convex, then  $g \circ h$  is convex.

*Proof.* For two arbitrary tensors  $\mathbf{A}, \mathbf{B} \in \mathbb{R}^{3 \times 3}$

$$(g \circ h)(\lambda \mathbf{A} + (1 - \lambda) \mathbf{B}) = g(h(\lambda \mathbf{A} + (1 - \lambda) \mathbf{B})) \quad (23)$$

$$\leq g(\lambda h(\mathbf{A}) + (1 - \lambda) h(\mathbf{B})) \quad \text{using convexity of } h \quad (24)$$

$$\leq \lambda g(h(\mathbf{A})) + (1 - \lambda) g(h(\mathbf{B})) \quad \text{using convexity of } g \quad (25)$$

$\square$

**Lemma 3** If  $\psi_1(I_1)$ ,  $\psi_2(I_2)$ , and  $\psi_3(I_3)$  are convex functions, then  $\psi = \psi_1(I_1) + \psi_2(I_2) + \psi_3(I_3)$  is polyconvex in  $\mathbf{F}$ .

*Proof.*  $I_1(\mathbf{F})$ ,  $I_2(\text{adj } \mathbf{F})$ , and  $I_3(\det \mathbf{F})$  are convex functions. Based on the composition lemma  $\psi_1(\mathbf{F})$ ,  $\psi_2(\text{adj } \mathbf{F})$ , and  $\psi_3(\det \mathbf{F})$  becomes convex as well. Hence,  $\psi$  is polyconvex in  $\mathbf{F}$ .  $\square$

In this work, the polyconvexity constraint is guaranteed by choosing parameterized functions for  $\psi_1(I_1)$  and  $\psi_2(I_2)$  which are convex and non-negative; will be clarified later. This additive structure is used in the unconstrained part the free energy Eq. (16), i.e.,  $\psi^{\text{uc}}(I_1, I_2) = \psi_1(I_1) + \psi_2(I_2)$ .

**Lemma 4** Affine transformation preserves the convexity.

*Proof.* Assuming the convexity of  $f(\mathbf{x})$  in  $\mathbf{x} \in \mathbb{R}^n$  and defining  $g(\mathbf{x}) = f(\mathbf{A}\mathbf{x} + \mathbf{b})$  where  $\mathbf{A} \in \mathbb{R}^{n \times n}$ ,  $\mathbf{b} \in \mathbb{R}^n$  are constants, then for two arbitrary  $\mathbf{x}_1, \mathbf{x}_2 \in \mathbb{R}^n$

$$g(\gamma \mathbf{x}_1 + (1 - \gamma) \mathbf{x}_2) = f(\mathbf{A}(\gamma \mathbf{x}_1 + (1 - \gamma) \mathbf{x}_2) + \mathbf{b}) \quad (26)$$

$$= f(\gamma(\mathbf{A}\mathbf{x}_1 + \mathbf{b}) + (1 - \gamma)(\mathbf{A}\mathbf{x}_2 + \mathbf{b})) \quad (27)$$

$$\leq \gamma f(\mathbf{A}\mathbf{x}_1 + \mathbf{b}) + (1 - \gamma) f(\mathbf{A}\mathbf{x}_2 + \mathbf{b}) \quad \text{using convexity of } f \quad (28)$$

$$= \gamma g(\mathbf{x}_1) + (1 - \gamma) g(\mathbf{x}_2) \quad (29)$$

$\square$

The affine transformation lemma guarantees that the usual linear data normalization (standardization) in machine learning such as `StandardScaler` and `MinMaxScaler` Pedregosa et al. [2011] do not alter the convexity results.

*Remark 2* Input data normalization is a practical technique to enhance the training of machine learning models Goodfellow et al. [2016], particularly when input or output has more than one feature. `StandardScaler` and `MinMaxScaler` are two common normalization methods. In `StandardScaler`, the input features are linearly mapped to have zero mean and unit standard deviation, i.e.,  $(\mathbf{x} - \boldsymbol{\mu}_x) / \boldsymbol{\sigma}_x$  where  $\boldsymbol{\mu}_x$  and  $\boldsymbol{\sigma}_x$  are mean and standard deviation per feature, respectively. In `MinMaxScaler`, the input features are linearly mapped to have zero min and unit max, i.e.,  $(\mathbf{x} - \mathbf{m}_x) / (\mathbf{M}_x - \mathbf{m}_x)$  where  $\mathbf{m}_x$  and  $\mathbf{M}_x$  are minimum and maximum values per feature, respectively.

### 2.2.6 Coercivity (growth) conditions

As mentioned earlier, certain coercivity (growth) conditions along with the polyconvexity results in the existence of the global minimizers. These conditions ensure that infinite strains result in unbounded stresses. The growth condition is satisfied if,

$$\psi(\mathbf{F}) \geq \alpha (\|\mathbf{F}\|^p + \|\text{adj}\mathbf{F}\|^q + (\det \mathbf{F})^r) + \beta, \quad (30)$$

for  $\alpha > 0$ ,  $\beta > 0$ ,  $p \geq 2$ ,  $q \geq \frac{p}{p-1}$ ,  $r > 1$ . The matrix norm is  $\|\mathbf{F}\|^2 = \text{tr}(\mathbf{F}^T \mathbf{F})$ . For the incompressible materials, this inequality can be simplified to,

$$\psi(\mathbf{F}) \geq \alpha(I_1^p + I_2^q) + \alpha + \beta, \quad (31)$$

In this work, we do not explicitly enforce coercivity condition, however, we will check the admissibility of the discovered equations according to the coercivity conditions.

*Remark 3* Compressing material towards zero volume should require infinite amount of energy. Thus one needs to enforce  $\psi \rightarrow \infty$  when  $J \rightarrow 0^+$  if the material is compressible.

### 2.2.7 Stress Free and Positivity conditions

In a general setup, the free energy function should be non-negative, produce stress free reference configuration when  $\mathbf{C} = \mathbf{F} = \mathbf{I}$ , i.e.,

$$W(\mathbf{F}) \geq 0, \quad (32)$$

$$W(\mathbf{I}) = 0, \quad \mathbf{S}(\mathbf{I}) = \mathbf{0}. \quad (33)$$

The non-negative condition can be satisfied by selecting parameterized free energy functions which are always positive and non-decreasing; will be introduced later.

### 2.2.8 Specific Form of Hyperelastic Energy Functional for Model Discovery

To ensure the zero stress state for the incompressible isotropic materials, we propose the following free energy function:

$$\psi^{\text{final}}(I_1, I_2) = \underbrace{\psi_1(I_1) + \psi_2(I_2)}_{\psi(I_1, I_2)} - \underbrace{\frac{1}{2}p(I_3 - 1)}_{\text{incompressibility}} - \underbrace{\alpha_0(I_3 - 1)}_{\psi_{P_0} \text{ zero stress}} - \underbrace{(\psi_1(3) + \psi_2(3))}_{\psi_0 \text{ zero energy}} \quad (34)$$

where  $\psi_{P_0}(I_3)$  is designed to enforce zero stress condition and,

$$\alpha_0 = \frac{d\psi_1}{dI_1} \Big|_{I_1=3} + 2 \frac{d\psi_2}{dI_2} \Big|_{I_2=3}. \quad (35)$$

One can straightforwardly show that the constructed strain energy satisfies zero stress conditions at the zero state, i.e., when  $I_1 = I_2 = 3$ ,  $I_3 = 1$ , and  $p = 0$ . As such, we will formulate the supervised learning problem such that the resultant expression is compatible with the form in Eq. (34). As we will discuss in latter section, this setting limits the expression trees included in the combinatoric optimization and hence reduces the difficulty of the symbolic regression problem.

### 3 Interpretable Model Discovery Compatible with Physical Constraints

Deriving a physics-constrained model consistent with the proposed form Eq.(34) directly through a single symbolic regression algorithm remains challenging for the following reasons. Firstly, it is challenging to straightforwardly restrict each expression tree to yield a convex function over the entire data range and beyond. Ensuring convexity constraints can be complex and may lead to sub-optimal results. Secondly, as illustrated in Figure 1, the stress objective function requires access to the gradient of the energy functional. This requirement can significantly increase the computational time of the symbolic regression, especially when dealing with deep expression trees with many terms. Finally, there is a high likelihood of encountering expression trees with non-stable functions, thus further complicating the symbolic regression training process.

To overcome this well-known challenge for symbolic regression, we modify our recently developed interpretable data-driven approach for uncovering plasticity yield surfaces Bahmani et al. [2023] such that the learning process is now taking account of the physics constraints. Our divide (step 1 in Figure 1) and conquer (step 2 in Figure 1) strategy still aims to merge the scalability of training neural-network models with the interpretability offered by symbolic regression. However, instead of deducing a model consistent with just the data, we establish a theoretical link between this computational approach and the classical findings of polyconvexity in the energy functional of isotropic hyperelasticity, which features an additive structure, as stated in Lemma 1.

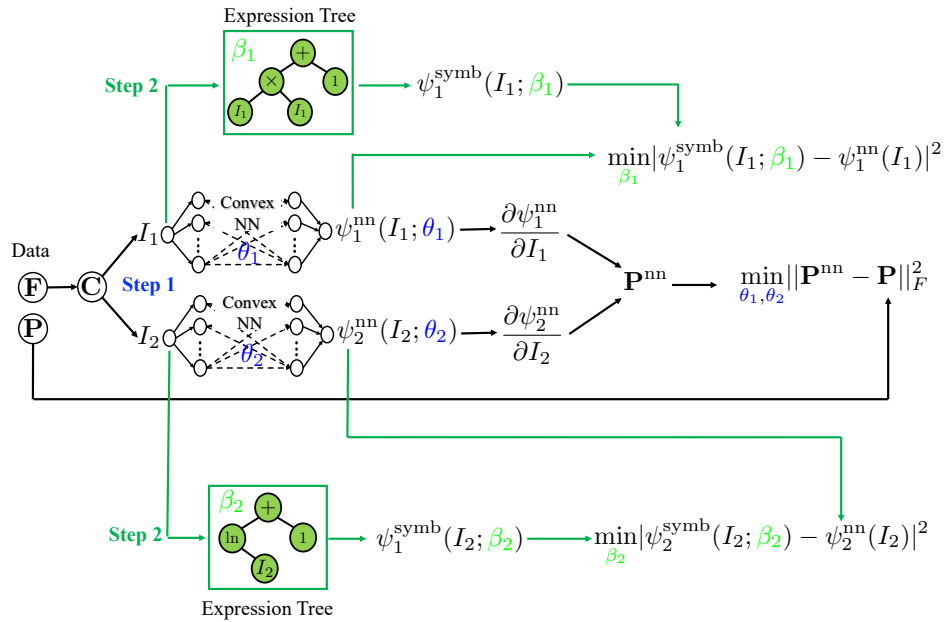


Fig. 1: The proposed interpretable hyperelastic model discovery by a two-step approach. In the **step 1**, a polyconvex neural additive model is trained by a **scalable** gradient-based optimizer multivariate hyperelasticity data. In the **step 2**, an evolutionary-based optimizer finds **interpretable** symbolic equations by conducting symbolic regression over univariate functions and in parallel. Data is assumed to be available in the form strain stress pair  $(\mathbf{F}, \mathbf{P})$ . Trainable neural network parameters are shown by blue color, i.e.,  $\beta_1, \beta_2$ . The unknown structure of the expression trees are shown by green color, i.e.,  $\beta_1, \beta_2$ , which are found by an evolutionary-based algorithm.

### 3.1 Polyconvex Neural Additive Model

Each shape function  $\psi_i(I_i)$  is parameterized by a separate neural network which must be convex, positive, and non-decreasing. A particular class of neural networks known as input-convex neural networks (ICNN) is designed by Amos et al. [Amos et al. \[2017\]](#) that fulfils all these properties.

The forward operations  $\psi^{ICNN}(I; \theta)$  in ICNN follows,

$$\mathbf{h}_1 = g_0(I\mathbf{v}^0 + \mathbf{b}^0); \quad \mathbf{v}^0, \mathbf{b}^0, \mathbf{h}^1 \in \mathbb{R}^{l_1}, \quad (36)$$

$$\mathbf{h}_{j+1} = g_j(\mathbf{W}^j \mathbf{h}^j + I\mathbf{v}^j + \mathbf{b}^j); \quad \mathbf{v}^j, \mathbf{b}^j, \mathbf{h}^j \in \mathbb{R}^{l_{j+1}}, \mathbf{W}^j \in \mathbb{R}^{+l_j \times l_{j+1}}, 1 \leq j < L \quad (37)$$

$$\psi^{ICNN} = h_L, \quad (38)$$

where  $L$  is the number of hidden layers, as shown in Figure 2,  $g_j$  are activation functions for each layer,  $h_j$  is the hidden representation of data at each layer, and  $\mathbf{W}^j$ ,  $\mathbf{b}^j$ , and  $\mathbf{v}^j$  are unknown, trainable parameters of the neural network.

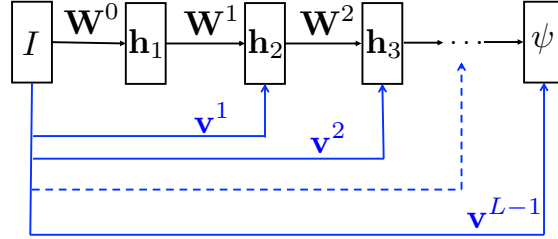


Fig. 2: Convex Neural Network which is guaranteed to be convex with respect to input  $I$ , non-decreasing and non-negative  $\psi > 0$  by construction.

**Proposition 1** *The function  $\psi^{ICNN}(I, \theta)$  is convex with respect to the input  $I$  if all  $\mathbf{W}^j$  are non-negative, and all activation functions  $g_j$  are convex.*

*Proof.* For the sake of completeness, we provide a straightforward proof. The first step in Equation (36) establishes the convexity of each component in the vector  $\mathbf{h}_1$ , see Lemmas 4 and 2. To verify the proposition, we must demonstrate the convexity of each component of  $\mathbf{h}_{j+1}$  with respect to  $I$  for  $j \geq 1$ . Equation (37) confirms this, as each component of the resulting vector  $\mathbf{W}^j \mathbf{h}^j$  is convex, see Lemma 5.  $\square$

**Lemma 5** *Weighted sum of convex functions  $h_i(x)$  with non-negative weights  $w_i$  results in convex function in  $x \in \mathbb{R}$ .*

*Proof.* Lets' define  $g(x) = w_i h_i(x)$  with constants  $w_i \in \mathbb{R}^+$  and convex functions  $h_i$ , for any arbitrary  $x_1, x_2, \lambda$  we have, with summation over  $i$ ,

$$g(\lambda x_1 + (1 - \lambda)x_2) = w_i h_i(\lambda x_1 + (1 - \lambda)x_2) \quad (39)$$

$$\leq w_i [\lambda h_i(x_1) + (1 - \lambda)h_i(x_2)] \quad \text{via convexity of } h_i \text{ and positivity } w_i \quad (40)$$

$$= \lambda w_i h_i(x_1) + (1 - \lambda)w_i h_i(x_2) \quad (41)$$

$$= \lambda g(x_1) + (1 - \lambda)g(x_2). \quad (42)$$

$\square$

*Remark 4* In this study, we utilize the softplus and softplus2 activation functions, both of which are convex and smooth. The functions are defined as follows:

$$\text{softplus}(x) = \ln(1 + \exp(x)), \quad (43)$$

$$\text{softplus2}(x) = \text{softplus}(x)^2. \quad (44)$$

The previous work [Klein et al., 2022, As'ad et al., 2022, Kalina et al., 2023] demonstrated the application of these activation functions in the context of ICNN modeling of hyperelastic energy functional.

### 3.2 Objective Function For Neural Network Training

Each shape function  $\psi_i(I_i)$  in Eq. (34) is parametrized by different ICNN  $\psi_i^{ICNN}(I_i; \theta^i)$  where  $\theta^i$  concatenates all trainable parameters associated with the  $i$ -th ICNN. In this work, we assume we only have access to strain and stress measurements stored for example as the dataset  $\mathcal{D} = \{\mathbf{F}^k, \mathbf{P}^k\}_{k=1}^{N_{\text{data}}}$  for  $N_{\text{data}}$  number of measurements. Notice that in realistic experiments, access to the values of energy functional or its Hessian is not possible although one may obtain them from numerical simulation.

To calibrate parameters  $\theta = \{\theta^i\}_{i=1}^2$ , we minimize the following loss function,

$$\theta = \arg \min_{\theta} \sum_{k=1}^{N_{\text{data}}} \left\| \frac{\partial \psi^{\text{tot}}(I_1, I_2; \theta)}{\partial \mathbf{F}} \Big|_{\mathbf{F}^k} - \mathbf{P}^k \right\|_F^2, \quad (45)$$

where  $\|\cdot\|_F$  is the Frobenius norm for the second order tensor. We use ADAM algorithm Kingma and Ba [2014] to minimize this single objective loss function.

### 3.3 Symbolic Regression

Symbolic regression (SR) aims to identify a mathematical expression that optimally fits a provided dataset without predefining the expression's form. The set of possible expressions is typically defined by establishing a range of mathematical operators, functions, variables, and constants, which are then efficiently represented using binary trees (refer to Fig. 3). Genetic programming is a widely adopted stochastic optimization technique for exploring the combinatorial space encompassing all conceivable mathematical expressions [Koza, 1994, Wang et al., 2019]. Moreover, recent advancements have been in utilizing deep reinforcement learning methods, offering alternative and efficient means for discrete searches within the domain of tree data structures [Petersen et al., 2019, Landajuela et al., 2021].

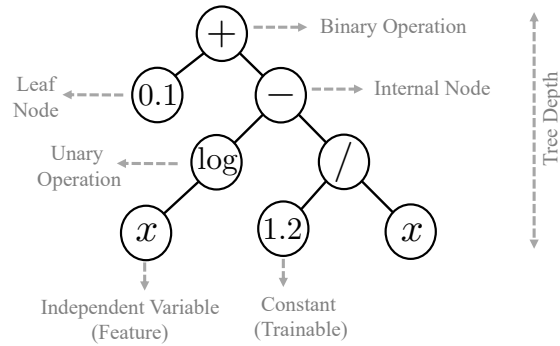


Fig. 3: Expression binary tree for equation representation. Program  $\log(x) - \frac{1.2}{x} + 0.1$  is represented by an expression tree with depth 3 and size 8 (total number of nodes).

Genetic programming employs a population of candidate solutions, randomly generated at the algorithm's start, to represent the space of potential expressions. Each individual candidate solution is described as an expression binary tree (refer to Figure 3), where the leaves symbolize input variables or constants, and the internal nodes denote mathematical operations or functions. The algorithm evaluates the fitness of each candidate solution by comparing its output to the target output values. In this study, we use mean square error (MSE) as the fitness measure, i.e.,

$$\text{MSE}(y^{\text{model}}, y^{\text{data}}) = \frac{1}{N_{\text{data}}} \sum_{i=1}^{N_{\text{data}}} (y_i^{\text{model}} - y_i^{\text{data}})^2. \quad (46)$$

The genetic programming algorithm utilizes an iterative process that evolves the population of candidate solutions through three main operators: selection, crossover, and mutation. This process draws inspiration from natural selection. In the selection step, the fittest individuals from the current population are chosen based on their fitness scores. Crossover (shown in Figure 4(a)) combines the genetic information of two individuals to generate offspring with characteristics inherited from both parents. On the other hand, mutation (depicted in Figure 4(b)) involves randomly altering some genetic material of an individual, thereby introducing new variations into the population.

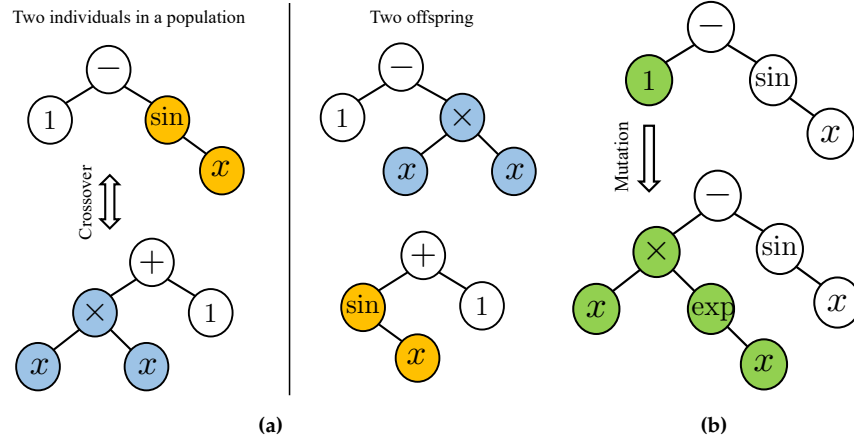


Fig. 4: (a) crossover and (b) mutation operations in an evolutionary-based symbolic regression algorithm.

The genetic programming algorithm creates improved candidate solutions iteratively until it finds a satisfactory mathematical expression that fits the data well. During SR optimization, there is a tradeoff between model complexity and expressivity. Striking a balance between the complexity and expressivity of the discovered analytical expression is vital to enhance interpretability and mitigate overfitting. Users can choose the best equation for their requirements, considering desired accuracy and simplicity.

**Definition 5 (Complexity score in symbolic regression)** The assessment of a symbolic equation's complexity is often qualitative due to the lack of a universally agreed-upon definition. In this study, we adopt the complexity measure proposed in Cranmer [2023], which uses the number of nodes in the expression tree as the complexity score. While assigning varying weights to different node types is feasible, such as considering  $\exp(\cdot)$  as more complex than  $+$ , we refrain from incorporating such weightings in our analysis.

Symbolic equations used in inference are lightweight compared to neural networks, making them more transportable. Research has shown that equations discovered by SR generalize well beyond the training data support, leading to successful training [Kim et al., 2020]. However, when dealing with multi-dimensional vector-valued or tensor-valued functions, symbolic regression becomes notably more challenging due to the complex combinatorial nature of the optimization problem involved in searching for

the appropriate mathematical expression [Icke and Bongard, 2013]. Our proposed method overcomes this concern, as mentioned earlier, by extracting a symbolic equation for each ICNN submodel, specifically for single-variable to single-variable data. This feature facilitates parallel computing, allowing SR algorithms to run simultaneously without any issues.

#### 4 Reduced forms for experimental calibration

Motivated by real experimental setups, we calibrate the model parameters for uni-axial extension, equibiaxial extension, and pure shear loading conditions in the incompressible limit. In this section, we summarize the reduced forms of equations for any general incompressible, isotropic free energy functional  $\psi(I_1, I_2)$  associated with each of these experimental boundary conditions.

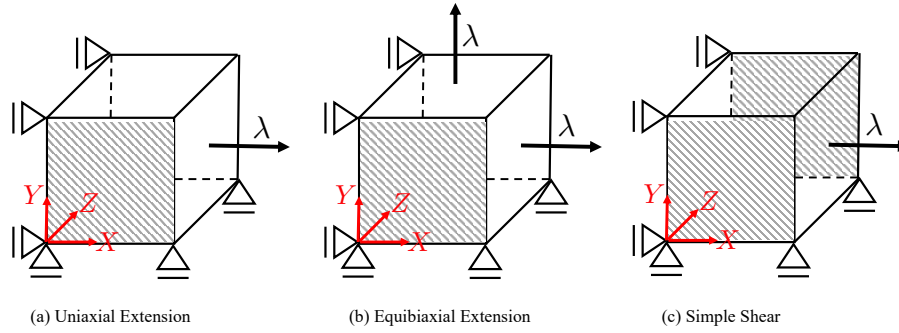


Fig. 5: Different loading conditions for the model calibration and training.

##### 4.1 Uniaxial Extension (UE)

The easiest experimental setup is UE where only one side of the cubic sample is deformed along its normal axis, e.g., X-axis shown in Fig. 5(a). Based on this condition, we only control for stretch  $\lambda_X = \lambda$ , but, due to the induced symmetry from isotropy, the other stretches are equal, and, hence from incompressibility they can be found  $\lambda_Y = \lambda_Z = \lambda^{-0.5}$ . Under these boundary conditions, only  $P_{11}$  becomes non-zero which can be found from Eqs. (16) and (34). In summary, the following reduced form is obtained for UE loading condition,

$$\mathbf{F} = \text{diag}(\lambda, \lambda^{-0.5}, \lambda^{-0.5}), \quad (47)$$

$$\mathbf{P} = \text{diag}(P_1, 0, 0), \quad (48)$$

$$P_1 = 2 \left( \frac{\partial \psi}{\partial I_1} + \frac{1}{\lambda} \frac{\partial \psi}{\partial I_2} \right) \left( \lambda - \frac{1}{\lambda^2} \right). \quad (49)$$

##### 4.2 Equibiaxial Extension (EBE)

EBE is similar to UE where extension loading is applied over two faces of the cubic sample as depicted in Fig. 5(b). Based on this condition, we control for stretches  $\lambda_X = \lambda_Y = \lambda$  and the other stretch is constrained to  $\lambda_Z = \lambda^{-2}$ , due to the incompressibility. Under these boundary conditions, only  $P_{11}$  and  $P_{22}$  become non-zero which are the same because of the induced symmetry of the isotropy condition. In summary, the

following reduced form is obtained for EBE loading condition,

$$\mathbf{F} = \text{diag}(\lambda, \lambda, \lambda^{-2}), \quad (50)$$

$$\mathbf{P} = \text{diag}(P_1, P_1, 0), \quad (51)$$

$$P_1 = 2 \left( \frac{\partial \psi}{\partial I_1} + \lambda^2 \frac{\partial \psi}{\partial I_2} \right) \left( \lambda - \frac{1}{\lambda^5} \right). \quad (52)$$

#### 4.3 Pure Shear (PS)

PS condition can be achieved by restricting the UE from any movement from the Z-axis, see Fig. 5(c). We control for stretches  $\lambda_X = \lambda$  and the other stretch is constrained to  $\lambda_Y = \lambda^{-1}$ . Under these boundary conditions, only  $P_{11}$  and  $P_{33}$  become non-zero. In summary, the following reduced form is obtained for PS loading condition,

$$\mathbf{F} = \text{diag}(\lambda, \lambda^{-1}, 1) \quad (53)$$

$$\mathbf{P} = \text{diag}(P_1, 0, P_3), \quad (54)$$

$$P_1 = 2 \left( \frac{\partial \psi}{\partial I_1} + \frac{\partial \psi}{\partial I_2} \right) \left( \lambda - \frac{1}{\lambda^3} \right), \quad (55)$$

$$P_3 = 2 \left( \frac{\partial \psi}{\partial I_1} + \lambda^2 \frac{\partial \psi}{\partial I_2} \right) \left( 1 - \frac{1}{\lambda^2} \right). \quad (56)$$

## 5 Numerical Examples

We demonstrate the application of our proposed method in discovering hyperelastic constitutive models through two examples. Firstly, in Section 5.1, we utilize experimental data from the literature to identify a material model. We compare the simplicity and accuracy of our discovered model with recent efforts in the field. Additionally, we assess and discuss the extrapolation capabilities of our method compared to a standard neural network approach.

In the second problem in Section 5.2, we showcase the method's potential in modeling more complex materials. To achieve this, we generate data using finite element simulations as a virtual experimental tool for a randomly synthesized particle-reinforced composite. Our discovered model will be compared to a ground-truth model available in the literature to validate its performance.

*Remark 5* Our framework is implemented in PyTorch [Paszke et al. \[2019\]](#) and PySR [Cranmer \[2023\]](#) open source packages for neural network and symbolic regression trainings, respectively.

### 5.1 Treloar's data for vulcanized rubber

In this example, we demonstrate the application of the proposed scheme in finding the hyperelastic energy functional for the well-known Treloar's experimental data on vulcanized rubber [Treloar \[1944\]](#). We compare the accuracy and simplicity of the discovered model with a reference model. Additionally, we highlight the significance of physics augmentation and interpretability in achieving better generalization compared to black-box neural network models.

We use 90% of Treloar's data for the model discovery algorithm and the remaining 10% is used for the model validation. Training related hyperparameters and setups are discussed in Appendix A.1. The discovered equation by the proposed algorithm is

$$\psi = c_{11} I_1 + c_{12} \exp(c_{13} I_1) + c_{21} I_2 + c_0, \quad (57)$$

where  $c_{11} = 0.1483$ ,  $c_{12} = 0.08155$ ,  $c_{13} = 0.066$ ,  $c_{21} = 0.00345$ , and  $c_0 = 294.8684$ . In Table 1, we compare its accuracy with another equation found by a recently introduced symbolic regression algorithm in [Abdusalamov et al. \[2023\]](#),

$$\psi_{\text{ref}} = \sqrt{0.93296 \exp(0.08031I_1) + \sqrt{I_1 - 0.080316} + (0.0232113I_1 + 0.021633)I_1}. \quad (58)$$

In this table,  $R^2$ -score is chosen as the measure of accuracy over the entire data.  $R^2$ -score between predicted values  $\{y_i\}_{i=1}^{N_{\text{data}}}$  and ground truth  $\{y_i^*\}_{i=1}^{N_{\text{data}}}$  is defined

$$R^2(y^*, y) = 1 - \frac{\sum_{i=1}^{N_{\text{data}}} (y_i^* - y_i)^2}{\sum_{i=1}^{N_{\text{data}}} (y_i^* - \text{mean}(y^*))^2}. \quad (59)$$

Based on this measure, our discovered equation shows improved performance in the EE dataset, with slight enhancements observed in the UE and PS datasets as well. Qualitatively, the discovered equation appears simpler, considering nested square root operators as more complex or in terms of the expression tree's depth. Additionally, in our work, we used 90% of the data to find the equation, whereas the reference utilized the entire dataset.

Table 1: Comparing  $R^2$  score for the discovered equation and the reference equation on Treloar's data.

Equation	Uniaxial Extension	Equibiaxial Extension	Pure Shear
This work Eq. (57)	0.9984	0.9899	0.9963
Reference Eq. (58)	0.9979	0.8692	0.9887

The trained input convex model  $\psi_1(I_1)$  for the polyconvex NAM solution  $\psi(I_1, I_2) = \psi_1(I_1) + \psi_2(I_2)$  is depicted in Figure 6, represented by the orange curve. The results for  $\psi_2(I_2)$  are omitted for brevity as it exhibits characteristics of a linear function, making it straightforward to handle. As mentioned earlier, in step 2 of the proposed method, we apply the SR algorithm to extract an equivalent symbolic equation for this learned model. The SQ training process takes less than 3 minutes on a MacBook Pro laptop with a Quad-Core Intel Core i5 processor running at 1.4 GHz and 16 GB of RAM. The SR algorithm lists several candidates ranked by their accuracy/simplicity, more accurate candidates are less simple.

In Figure 7, we present the accuracy vs. complexity plots for both the function  $\psi_1(I_1)$  and its gradient  $\psi_1'(I_1)$ . While the gradient information is not employed in the fitness measure utilized, we recommend considering this information for model selection during the post-processing step among all available candidates. This is crucial because the accuracy of the gradient directly impacts the final stress prediction, which relies on this information. We employ a selection criteria based on two factors: candidates with errors below a specified threshold and those exhibiting an abrupt accuracy improvement compared to their simpler counterparts; see the vertical red line in the figure. A comparison between the selected equation and the ICNN model is illustrated in Figure 6, with the symbolic equation depicted by blue curves. A good agreement between the ICNN model and the symbolic equation is observed. Moreover, the behavior of the symbolic function beyond the ICNN training data appears to be reasonable.

We further compare the proposed scheme with a vanilla neural network (NN)-based solution. In the case of vanilla NN, we substitute  $\psi(I_1, I_2)$  in Equation (34) with a conventional multilayer perceptron (MLP), accepting both  $I_1$  and  $I_2$  in its input layer. The model accuracy during the optimization iterations in step 1 for the polyconvex NAM and vanilla NN is illustrated in Figure 8 over the training and validation data. While the final loss value for the training curve in the case of vanilla NN is lower than that of the polyconvex NAM, its larger discrepancy between the validation and training curves indicates overfitting. This overfitting may lead to less reliable predictions in the extrapolation regime.

To assess the models' capabilities, we compare  $R^2$ -scores between the polyconvex NAM and vanilla NN across all three data sets, as shown in Figure 9. Both models exhibit satisfactory  $R^2$ -scores across all the available data. The polyconvex NN demonstrates better performance for UE and EBE, while the vanilla NN shows slightly better accuracy in the case of the PS data set. However, it is essential to note that we

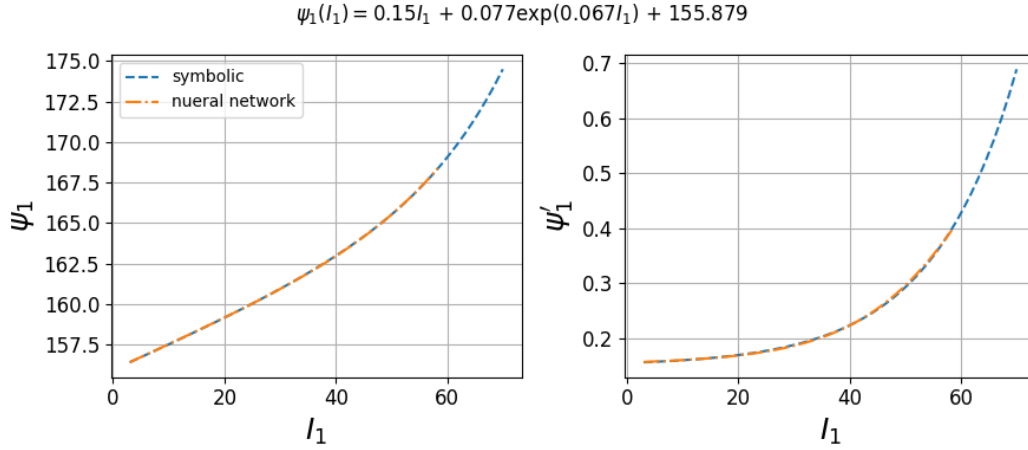


Fig. 6: Discovered symbolic function from trained neural network representation. Function and its gradient is shown in left and right plots, respectively. Data in training range (orange curves) is only used for the symbolic regression.

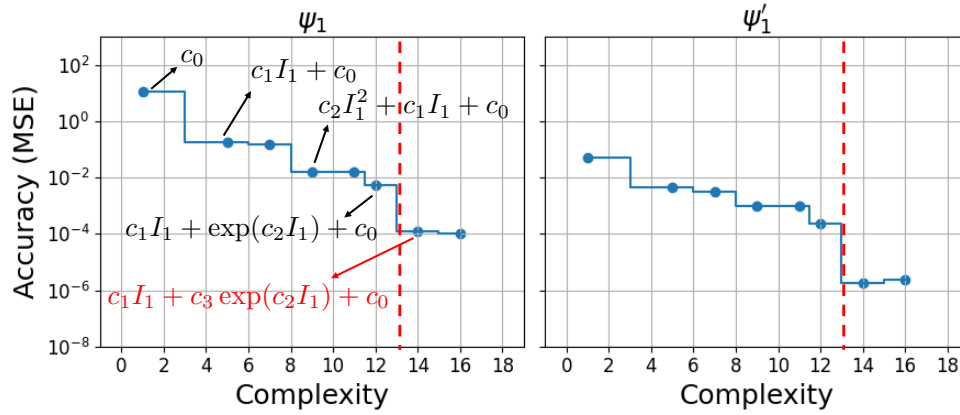


Fig. 7: Complexity (parsimony) vs accuracy for the function discovery and its gradient regarding Treloar's data. More complex equations have more terms. Achieving a balance between accuracy and simplicity is essential for both the function and its gradient.

observe non-physical behavior for the vanilla NN in the case of the EBE data set when moving beyond the training data regime.

In order to highlight the extrapolation power resulting from physics augmentation, simplicity, and interpretability of the proposed scheme, we compare the models' predictions of the symbolic equation discovered in this work (Equation (57)), the one found in the reference (Equation (58)), and the vanilla NN in Figure 10, where we extend far beyond the training data ranges. Given that we lack access to real data at these ranges, we cannot assess the accuracy of the symbolic equations. However, both equations exhibit reasonable behavior. On the other hand, the response of the vanilla NN is notably unacceptable, especially under EBE loading condition.

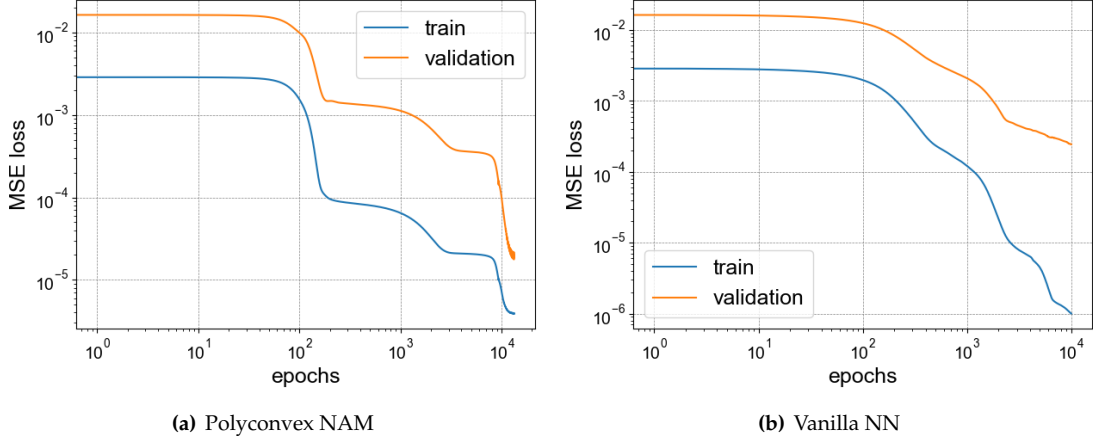


Fig. 8: Validation and training losses for model calibration in the step 1 where a neural network-based solution is searched. 90% of the data is utilized for training.

## 5.2 Particle-reinforced composite

In this example, we synthesize data through numerical experimentation on a fabricated particle-reinforced composite. This demonstration highlights the method's efficacy in handling more complex material behaviors. A cubic sample of the composite material with length 1cm is generated by random placement of hard particles in the soft matrix as shown in Figure 11. Neo-Hookean [Ogden \[1997\]](#) and the Exp-Log model [Khajehsaeid et al. \[2013\]](#) are assumed for the particles and the matrix, respectively,

$$\psi_{\text{NH}} = \frac{1}{2}\mu(I_1 - 3), \quad (60)$$

$$\psi_{\text{exp-log}} = A \left[ \frac{1}{a} \exp(a(I_1 - 3)) + b(I_1 - 1)(1 - \log(I_1 - 2)) - \frac{1}{a} - b \right], \quad (61)$$

where material parameters  $\mu = 0.5$  MPa,  $A = 0.195$  MPa,  $a = 0.018$ ,  $b = 0.33$ ; in the limit of small deformation  $A$  is analogous to the shear modulus  $\mu$  in the Neo-Hookean model. Uniaxial behavior of these constituents are shown in Figure 11(b).

We subject the composite to a uni-axial extension loading condition using a displacement control FEM simulator. During this process, we collect 64 data points with a displacement increment of 0.8 mm by recording the average forces calculated over the sample surface where the loads are applied; forces are used to compute stresses. The generated data set for training the models are depicted in Figure 12.

For training purposes, we utilize 75% of the data, represented by green circle points in Figure 12. The remaining portion of the data, which entirely lies in the extrapolation regime, is used as the validation dataset. The discovered equation by our method is,

$$\psi = c_{11}I_1 + c_{12}I_1^4 + \exp(c_{13}I_1) + c_{21}I_2 + c_{22}I_2^2 \ln(I_2) + c_0, \quad (62)$$

where  $c_{11} = 0.06948$ ,  $c_{12} = 1.82532 \times 10^{-6}$ ,  $c_{13} = -0.05967$ ,  $c_{21} = 0.91519$ ,  $c_{22} = 0.0069682$ ,  $c_0 = 15.87993107$ . The  $R^2$ -scores of this symbolic equation and the polyconvex NAM model are almost the same, with a slightly better performance of the polyconvex NAM model, as shown at the top of Figure 12. Additionally, the comparison between the symbolic representation of each of the learned ICNN models  $\psi_i(I_i)$  is presented in Figures 13 and 14. The results indicate good agreements between the function values and their gradients between the neural networks and symbolic equations.

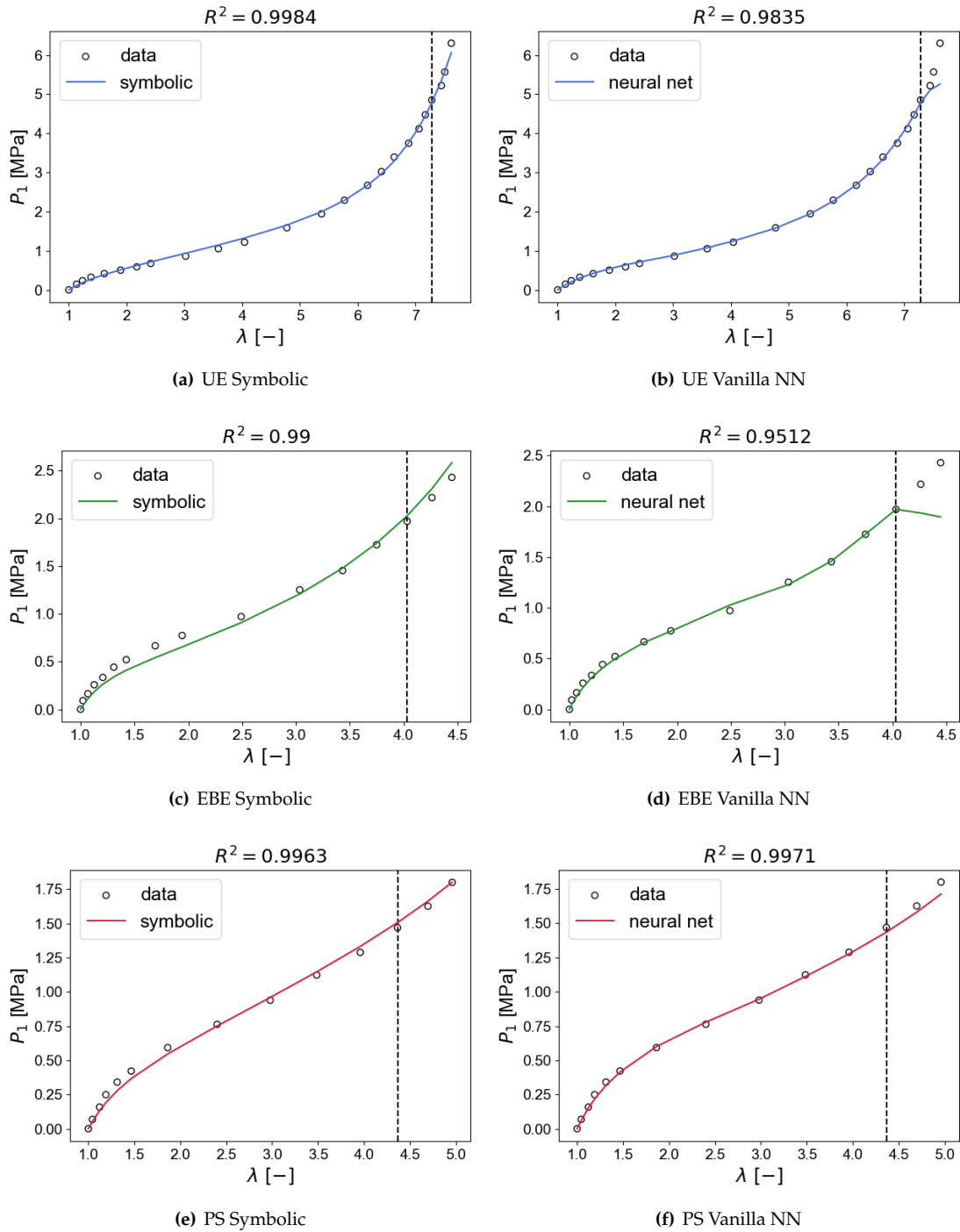


Fig. 9: Predictions via the discovered equation for Treloar's data. Vertical dashed line shows the training data region, beyond that is the validation data.  $R^2$  scores indicate the accuracy measure for the entire data (train and validation) in each experimental loading conditions. The training is conducted on all three loading conditions at the same time.

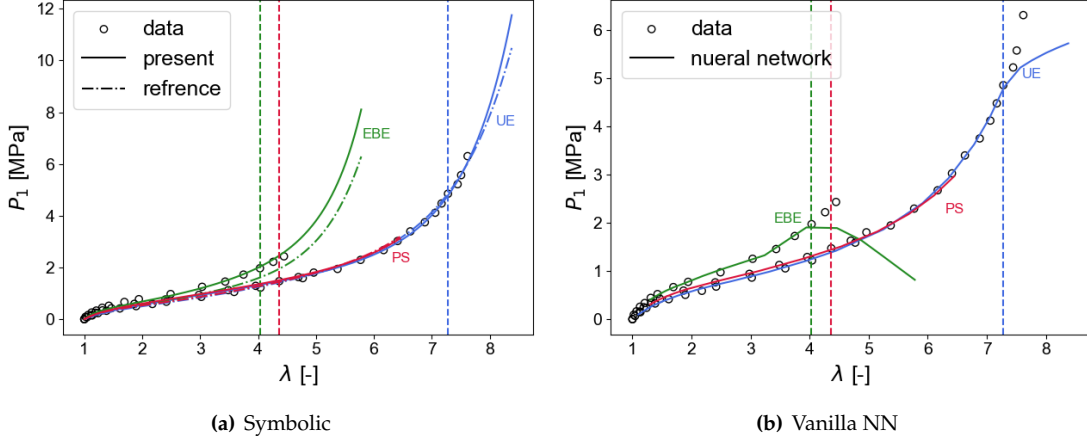


Fig. 10: Extrapolation capability via (a) the discovered symbolic equation, (b) vanilla nural network for Treloar's data. In (a), we compare results obtained by Eq. (57) and the reference Eq. (58). The vertical lines indicate the training regime utilized for model training. The discovered equation extrapolates well and shows slightly better accuracy than the reference equation. Predictions via vanilla neural networks are not accurate beyond the training data.

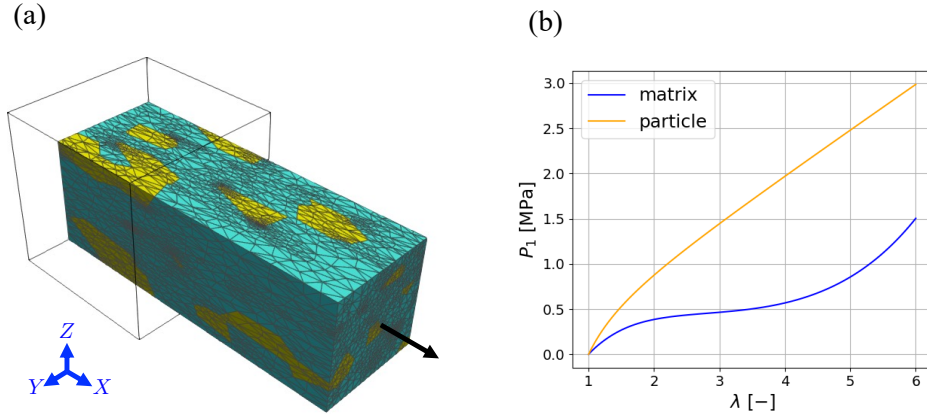


Fig. 11: (a) Particle-reinforced composite at longitudinal strain 100%. (b) uniaxial behavior of each constituent. In (a), random particles with total volume fraction 0.22 are shown by yellow color.

### 5.2.1 Remarks on model execution time

Another advantage of obtaining symbolic equations is their computational efficiency when compared to their neural network-based counterparts. In Figure 15, we compare the execution times for inference between the polyconvex neural additive model and symbolic regression. As anticipated, the runtime for symbolic calculations is shorter than that of neural network forward operations, primarily due to the reduced number of floating-point operations in the symbolic equation. While automatic differentiation provides implementation flexibility, it introduces additional overhead due to the construction of the computational graph, which can be avoided if symbolic operations are effectively managed manually.

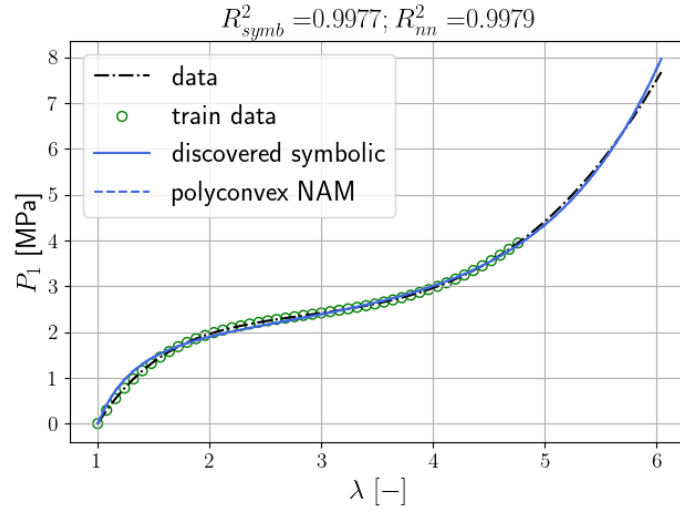


Fig. 12: Comparison between the discovered symbolic energy functional and the learned polyconvex NAM for particle-reinforced composite data.

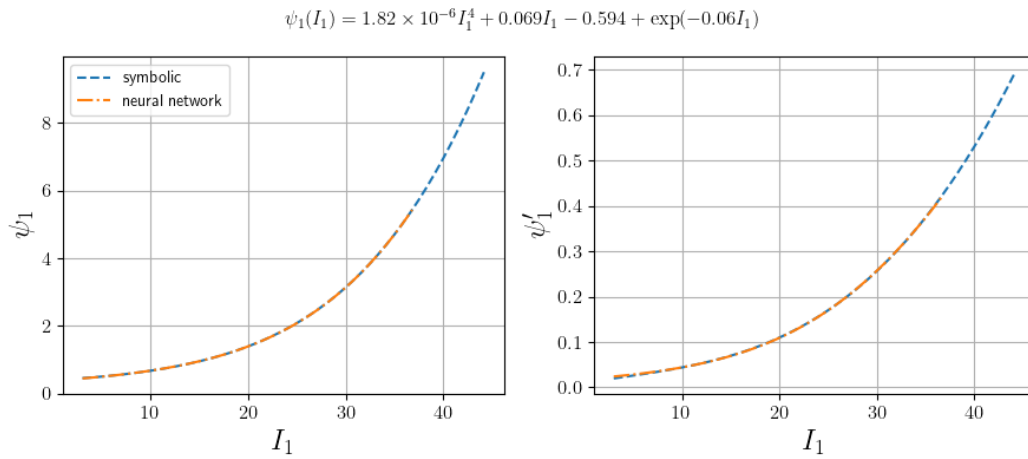


Fig. 13: Discovered symbolic function from trained neural network representation. Function and its gradient is shown in left and right plots, respectively. Data in training range (orange curves) is only used for the symbolic regression.

## 6 Discussion and Analysis

Thanks to the symbolic forms, classical analysis can be applied to investigate the entire range of the deformation gradient, determining when polyconvexity and growth conditions are violated. In our specific formulation, we can assess quasiconvexity by examining the convexity of shape functions  $\psi_i(I_i)$ . To verify coercivity, we analyze the energy functional's growth behavior as the invariants approach infinity, i.e.,  $I_1, I_2 \rightarrow \infty$ . It is important to note that our goal is not to find the tightest bounds on the coefficients, but rather to ensure that the derived equations satisfy the required conditions.

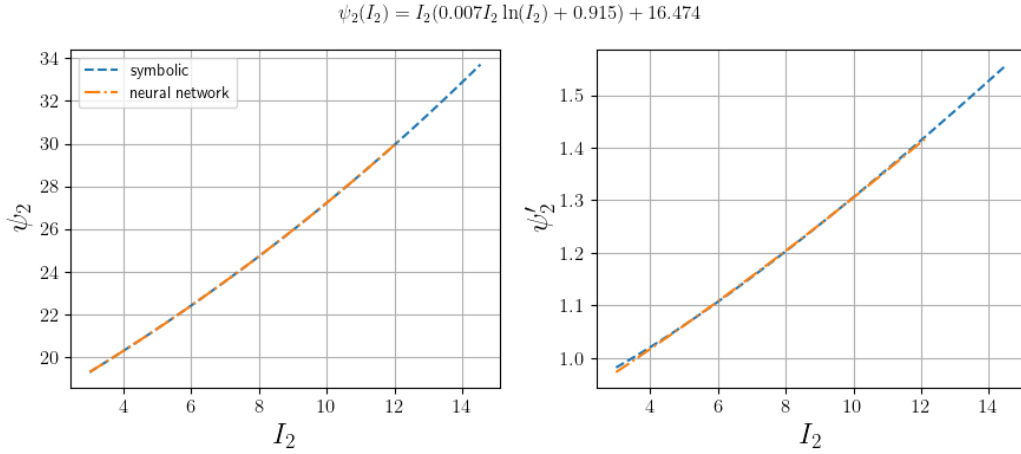


Fig. 14: Discovered symbolic function from trained neural network representation. Function and its gradient is shown in left and right plots, respectively. Data in training range (orange curves) is only used for the symbolic regression.

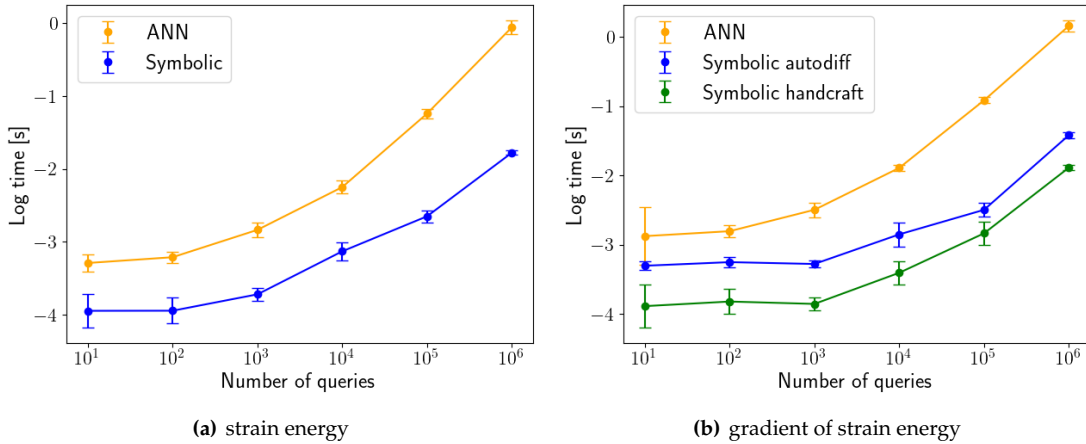


Fig. 15: Comparing execution times between a neural network and a symbolic strain energy functional. Mean and standard deviation trends for (a) strain energy calculation and (b) its gradient with respect to invariants. The gradient of a symbolic equation can be manually crafted or obtained through automatic differentiation, as showcased in (b). The horizontal axis represents the number of query points in each experiment. Each experiment is replicated 20 times with distinct random seeds.

### 6.1 Treloar Machine Learning Model

The convexity of  $\psi_2(I_2) = c_{21}I_2$  is evident. For  $\psi_1(I_1) = c_{11}I_1 + c_{12} \exp(c_{13}I_2)$  to be convex, it is required that  $c_{12} \geq 0$ , which can be confirmed by checking the positivity of its second-order derivative. By employing the Taylor series expansion for the exponential function and considering any positive integer  $p$ , we obtain the inequality:

$$\psi(I_1, I_1) \geq \frac{c_{12}^p}{p!} I_1^p + c_{21}I_2. \quad (63)$$

To ensure asymptotic satisfaction of Equation (31), we can set  $\alpha = \min(c_{12}^p/p!, c_{21})$  with  $c_{21} > 0$  and  $q = 1$ , where  $p$  is chosen to be a large value approaching infinity. However, it is essential to note that even for a very large  $p$ , the condition  $q \geq p/(p-1)$  is marginally violated, and the fulfillment of conditions  $c_{22} > 0$  and  $c_{12} > 0$  may not guarantee coercivity based on the presented justification.

*Remark 6* In this paper, our primary objective is not to perform a rigorous inequality analysis. Instead, we aim to highlight the distinctive capability of our data-driven model discovery approach, which distinguishes it from black-box methods. Our focus lies in showcasing the potential and effectiveness of our methodology, rather than engaging in extensive mathematical inequality analyses.

## 6.2 Particle-reinforced Composite Machine Learning Model

Convexity of  $\psi_1(I_1) = c_{11}I_1 + c_{12}I_1^4 + \exp(c_{13}I_1)$  is satisfied if its second order gradient is non negative, i.e.,  $12c_{12}I_1^2 + c_{13}^2 \exp(c_{13}I_1) \geq 0$ . Hence, it only requires that  $c_{12} \geq 0$ . Similarly, for the  $\psi_2(I_2) = c_{21}I_2 + c_{22}I_2^2 \ln(I_2)$ , the convexity requirement is  $c_{22}(2 \ln(I_2) + 3) \geq 0$  which is satisfied if  $c_{22} \geq 0$ .

Again considering Taylor series for the exponential function,

$$\psi_1(I_1) \geq c_{11}I_1 + c_{12}I_1^4 + \frac{c_{13}^4}{4!}I_1^4 \geq (c_{12} + \frac{c_{13}^4}{4!})I_1^4. \quad (64)$$

Using the fact that  $\ln(x) \geq \frac{x-1}{x}$  for positive  $x$  (since  $x \ln(x) - x + 1$  has positive slope), one can writes,

$$\psi_2(I_2) \geq c_{22}I_2^2 + (c_{21} - c_{22})I_2 \geq \hat{c}_{22}I_2^2, \quad (65)$$

where  $0 \leq \hat{c}_{22} \leq c_{22}$  to account for the possibility  $c_{21} < c_{22}$ .

Based on these bounds, if we choose

$$\alpha = \min(c_{12} + c_{13}^4/4!, \hat{c}_{22}), \quad (p = 4) \geq 2, \quad (q = 2) \geq (\frac{p}{p-1} = 1.3) \quad (66)$$

, the inequality Equation (31) is satisfied provided that  $\alpha > 0$ . So the sufficient conditions to satisfy coercivity are  $c_{22} > 0$  and  $c_{12} > 0$ .

The convexity of  $\psi_1(I_1) = c_{11}I_1 + c_{12}I_1^4 + \exp(c_{13}I_1)$  is ensured if its second-order gradient is non-negative, i.e.,  $12c_{12}I_1^2 + c_{13}^2 \exp(c_{13}I_1) \geq 0$ . Thus, it requires only that  $c_{12} \geq 0$  to satisfy convexity. Similarly, for  $\psi_2(I_2) = c_{21}I_2 + c_{22}I_2^2 \ln(I_2)$ , the convexity requirement is  $c_{22}(2 \ln(I_2) + 3) \geq 0$ , which is satisfied if  $c_{22} \geq 0$ .

By utilizing the Taylor series expansion for the exponential function, we have:

$$\psi_1(I_1) \geq c_{11}I_1 + c_{12}I_1^4 + \frac{c_{13}^4}{4!}I_1^4 \geq (c_{12} + \frac{c_{13}^4}{4!})I_1^4. \quad (67)$$

Furthermore, leveraging the fact that  $\ln(x) \geq \frac{x-1}{x}$  for positive  $x$  (as  $x \ln(x) - x + 1$  has a positive slope), we can write:

$$\psi_2(I_2) \geq c_{22}I_2^2 + (c_{21} - c_{22})I_2 \geq \hat{c}_{22}I_2^2, \quad (68)$$

where  $0 \leq \hat{c}_{22} \leq c_{22}$  accounts for the possibility of  $c_{21} < c_{22}$ .

Based on these bounds, if we choose  $\alpha = \min(c_{12} + c_{13}^4/4!, \hat{c}_{22})$ , set  $p = 4 \geq 2$ , and  $q = 2 \geq p/(p-1)$ , the inequality Equation (31) is satisfied, provided that  $\alpha > 0$ . Consequently, the sufficient conditions to ensure coercivity are  $c_{22} > 0$  and  $c_{12} > 0$ .

## 7 Conclusion

In this work, we present an efficient machine learning framework capable of directly infer the mathematical expressions of multivariate elastic stored energy functional models from data that fulfill physics principle (e.g. polyconvexity, material frame indifference) without sacrificing expressivity. A salient feature of this proposed model is the introduction of the input convex neural network for constructing the feature space. This treatment enables us to retain the convexity of the feature mapping that ensures polyconvexity of the learned neural network hyperelasticity model. By expressing polyconvex hyperelasticity model in the feature space, we can then apply symbolic regression on each of the feature space basis sequentially. This setting enables us to overcome the challenging curse-of-high-dimensionality issue well known in the symbolic regression literature while deducing interpretable mathematical model that can be easily comprehended, analyzed, and implemented. The compactness of the mathematical model also lead to computationally efficient constitute update that requires less arithmetic operation than those of the deep neural nets and hence well-suited for large-scale physics simulations where repeated execution of the models must be carried out in a large number of integration points.

## Acknowledgement

The authors is grateful for the supports provided by the UPS foundation and the department of civil and environmental engineering of Stanford University that enables the authors to complete this manuscript at the Stanford campus. The authors are supported by the National Science Foundation under grant contracts CMMI-1846875, and the Dynamic Materials and Interactions Program from the Air Force Office of Scientific Research under grant contracts FA9550-21-1-0391 and FA9550-21-1-0027, and the MURI Grant No. FA9550-19-1-0318. These supports are gratefully acknowledged. The views and conclusions contained in this document are those of the authors, and should not be interpreted as representing the official policies, either expressed or implied, of the sponsors, including the U.S. Government. The U.S. Government is authorized to reproduce and distribute reprints for Government purposes notwithstanding any copyright notation herein. The views and conclusions contained in this document are those of the authors, and should not be interpreted as representing the official policies, either expressed or implied, of the sponsors, including the Army Research Laboratory or the U.S. Government. The U.S. Government is authorized to reproduce and distribute reprints for Government purposes notwithstanding any copyright notation herein.

## Data Availability Statement

The data supporting the findings of this study are available will be available at Mendeley Data upon the acceptance of this manuscript. The code used to generated the model will be available at GitHub upon the acceptance of this manuscript as well.

## Appendix A Model Setup and Hyperparametrs

In the polyconvex NAM model, both examples employ each shape function with the ICNN model using a single hidden layer consisting of 50 neurons. The activation functions for the first and second layers are softplus and softplus2, respectively. To ensure non-negativity of weights, ReLU activation is utilized. The optimization process utilizes the ADAM optimizer with an initial learning rate of 0.001. Strain invariants are normalized using the MinMaxScaler method in both examples. Furthermore, in the first example, the stress data undergoes a pre-processing step and is scaled by a factor of 0.05.

### A.1 Treloar's data

In the vanilla NN model, one hidden layer with 50 neurons is utilized with ELU activation layer [Clevert et al. \[2015\]](#), see the following remark. The training parameters remain consistent with that of the polyconvex NAM model.

In the SR configuration of  $\psi_1(I_1)$ , we confine the binary operators to addition and multiplication, while the unary operator is limited to the exponential function (exp). The time budget is capped at 6 minutes, or a maximum of 100 iterations, whichever comes first. The expression trees' maximum depth and size are both set to 30. As a result of the observed simplicity in the learned ICNN function for  $\psi_2(I_2)$ , the maximum size and depth of expression tree searches have been reduced to 10, and the exponential function has been excluded as a possible operator for applying the SR to  $\psi_2(I_2)$ .

*Remark 7* The ELU activation function is defined as follows:

$$\text{ELU}(x) = xH(x) + (\exp(x) - 1)(1 - H(x)), \quad (69)$$

where  $H(x)$  is the Heaviside function.

### A.2 Composite data

In the SR configuration of  $\psi_1(I_1)$ , the binary operators are restricted to addition and multiplication, and the unary operators are limited to the exponential (exp) and logarithm (ln) functions. The time budget is set at 6 minutes or a maximum of 100 iterations, whichever is reached first. The expression trees are constrained to a maximum depth of 10 and a size of 50. Classical energy functionals rarely employ nested ln or exp operators; therefore, during the SR iterations, we exclude the possibility of such combinations.

A similar SR configuration is employed for  $\psi_2(I_2)$  with the following differences: the expression tree has a maximum size of 15 and a maximum depth of 5.

## Appendix B Finite Element Discretization

For ease of implementation, we use penalty approach to weakly impose the incompressibility. Although this method does not enforce the incompressibility exactly, it leads to a simple system of nonlinear equations based on solely the displacement field. Other multi-field formulations are possible but they are computationally more demanding which is not considered in this work [[Weiss et al., 1996](#), [Schröder et al., 2017](#)].

For numerical stability reasons, one may prefer to additively decompose strain energy functional to volumetric  $\psi_{\text{vol}}$  and deviatoric  $\psi_{\text{dev}}$  parts, i.e.,  $\psi(\mathbf{C}) = \psi_{\text{dev}}(\bar{\mathbf{C}}) + \psi_{\text{vol}}(J)$ . In the near-incompressibility regime, the volumetric part acts as a penalty term to enforce  $|J - 1| < \epsilon$ . In this work, the penalty term is chosen as follows,

$$\psi_{\text{vol}} = \frac{1}{2}\kappa \ln^2(J), \quad (70)$$

where  $\kappa$  is the penalty parameter. Higher value of this parameter enforces the incompressibility more precisely, however for numerical instability issues one may need to choose it reasonably high. The deviatoric part of the right Cauchy-Green is defined,

$$\bar{\mathbf{C}} = J^{-\frac{2}{3}}\mathbf{C}. \quad (71)$$

The unknown displacement field  $\mathbf{U}(\mathbf{X})$  defined over the undeformed domain  $\Omega_0$  is the stationary point of the total energy functional when neglecting body forces and non-zero traction boundary conditions,

$$\mathbf{U} = \arg \min_{\mathbf{U}} \Pi(\mathbf{U}(\mathbf{X})), \quad (72)$$

$$\Pi(\mathbf{U}) = \int_{\Omega_0} \psi(\mathbf{U}(\mathbf{X})) d\Omega. \quad (73)$$

To find the minima, we discretize the domain using hexahedral elements and use linear basis functions for the displacement field,

$$\Pi(\mathbf{U}) \approx \Pi(\bar{\mathbf{U}}) = \sum_{i=1}^{N_{\text{elem}}} \int_{\Omega_i^e} \psi \left( \mathbf{N}^T(\mathbf{X}) \bar{\mathbf{U}} \right) d\Omega, \quad (74)$$

where interpolation using FE basis is utilized, i.e.,  $\mathbf{U} = \mathbf{N}^T(\mathbf{X})\bar{\mathbf{U}}$ , and  $\mathbf{N}$  is the linear basis function for the vector field in 3D. The element-level integration is performed using the second-order quadrature rule. To solve the nonlinear system of equations based on the nodal displacement  $\bar{\mathbf{U}}$ , we employ the Newton-Raphson method. For more detailed information, readers are referred to Belytschko et al. [2014]. Our implementation is carried out using FEniCS Alnæs et al. [2015].

## References

- Rasul Abdusalamov, Markus Hillgärtner, and Mikhail Itskov. Automatic generation of interpretable hyperelastic material models by symbolic regression. *International Journal for Numerical Methods in Engineering*, 124(9):2093–2104, 2023.
- Rishabh Agarwal, Levi Melnick, Nicholas Frosst, Xuezhou Zhang, Ben Lengerich, Rich Caruana, and Geoffrey E Hinton. Neural additive models: Interpretable machine learning with neural nets. *Advances in neural information processing systems*, 34:4699–4711, 2021.
- Ramin Akbari, Vahid Morovati, and Roozbeh Dargazany. Reverse physically motivated frameworks for investigation of strain energy function in rubber-like elasticity. *International Journal of Mechanical Sciences*, 221:107110, 2022.
- Martin Alnæs, Jan Blechta, Johan Hake, August Johansson, Benjamin Kehlet, Anders Logg, Chris Richardson, Johannes Ring, Marie E Rognes, and Garth N Wells. The fenics project version 1.5. *Archive of numerical software*, 3(100), 2015.
- Víctor Jesús Amores, José María Benítez, and Francisco Javier Montáns. Average-chain behavior of isotropic incompressible polymers obtained from macroscopic experimental data. a simple structure-based wpyiwyg model in julia language. *Advances in Engineering Software*, 130:41–57, 2019.
- Brandon Amos, Lei Xu, and J Zico Kolter. Input convex neural networks. In *International Conference on Machine Learning*, pages 146–155. PMLR, 2017.
- Faisal As’ad, Philip Avery, and Charbel Farhat. A mechanics-informed artificial neural network approach in data-driven constitutive modeling. *International Journal for Numerical Methods in Engineering*, 123(12):2738–2759, 2022.
- Bahador Bahmani and WaiChing Sun. Training multi-objective/multi-task collocation physics-informed neural network with student/teachers transfer learnings. *arXiv preprint arXiv:2107.11496*, 2021.
- Bahador Bahmani and WaiChing Sun. Manifold embedding data-driven mechanics. *Journal of the Mechanics and Physics of Solids*, 166:104927, 2022.
- Bahador Bahmani and WaiChing Sun. Distance-preserving manifold denoising for data-driven mechanics. *Computer Methods in Applied Mechanics and Engineering*, 405:115857, 2023.
- Bahador Bahmani, Hyung Suk Suh, and WaiChing Sun. Discovering interpretable elastoplasticity models via the neural polynomial method enabled symbolic regressions. *arXiv preprint arXiv:2307.13149*, 2023.
- John M Ball. Convexity conditions and existence theorems in nonlinear elasticity. *Archive for rational mechanics and Analysis*, 63:337–403, 1976.
- John M Ball. Strict convexity, strong ellipticity, and regularity in the calculus of variations. In *Mathematical Proceedings of the Cambridge Philosophical Society*, volume 87, pages 501–513. Cambridge University Press, 1980.
- John M Ball. Does rank-one convexity imply quasiconvexity? In *Metastability and incompletely posed problems*, pages 17–32. Springer, 1987.
- Daniele Barbani, Niccolò Baldanzini, and Marco Pierini. Development and validation of an fe model for motorcycle-car crash test simulations. *International journal of crashworthiness*, 19(3):244–263, 2014.
- Ted Belytschko, Wing Kam Liu, Brian Moran, and Khalil Elkhodary. *Nonlinear finite elements for continua and structures*. John wiley & sons, 2014.

- GF Bomarito, TS Townsend, KM Stewart, KV Esham, JM Emery, and JD Hochhalter. Development of interpretable, data-driven plasticity models with symbolic regression. *Computers & Structures*, 252:106557, 2021.
- Mary C Boyce and Ellen M Arruda. Constitutive models of rubber elasticity: a review. *Rubber chemistry and technology*, 73(3):504–523, 2000.
- Michael M Bronstein, Joan Bruna, Taco Cohen, and Petar Veličković. Geometric deep learning: Grids, groups, graphs, geodesics, and gauges. *arXiv preprint arXiv:2104.13478*, 2021.
- Steven L Brunton, Joshua L Proctor, and J Nathan Kutz. Discovering governing equations from data by sparse identification of nonlinear dynamical systems. *Proceedings of the national academy of sciences*, 113(15):3932–3937, 2016.
- Chen Cai, Nikolaos Vlassis, Lucas Magee, Ran Ma, Zeyu Xiong, Bahador Bahmani, Teng-Fong Wong, Yusu Wang, and WaiChing Sun. Equivariant geometric learning for digital rock physics: estimating formation factor and effective permeability tensors from morse graph. *International Journal for Multiscale Computational Engineering*, 21(5), 2023.
- Peiyi Chen and Johann Guilleminot. Polyconvex neural networks for hyperelastic constitutive models: A rectification approach. *Mechanics Research Communications*, 125:103993, 2022.
- Djork-Arné Clevert, Thomas Unterthiner, and Sepp Hochreiter. Fast and accurate deep network learning by exponential linear units (elus). *arXiv preprint arXiv:1511.07289*, 2015.
- Miles Cranmer. Interpretable machine learning for science with pysr and symbolic regression. *jl. arXiv preprint arXiv:2305.01582*, 2023.
- José Crespo, Marcos Latorre, and Francisco Javier Montáns. Wpiwyg hyperelasticity for isotropic, compressible materials. *Computational Mechanics*, 59:73–92, 2017.
- YF Dafalias. Modelling cyclic plasticity; simple versus sophistication. *Mechanics of Engineering Materials (John Wiley & Sons, New York, 1984) pp*, pages 153–178, 1984.
- Judith E Dayhoff and James M DeLeo. Artificial neural networks: opening the black box. *Cancer: Interdisciplinary International Journal of the American Cancer Society*, 91(S8):1615–1635, 2001.
- Mauricio Fernández, Felix Fritzen, and Oliver Weeger. Material modeling for parametric, anisotropic finite strain hyperelasticity based on machine learning with application in optimization of metamaterials. *International Journal for Numerical Methods in Engineering*, 123(2):577–609, 2022.
- Moritz Flaschel, Siddhant Kumar, and Laura De Lorenzis. Unsupervised discovery of interpretable hyperelastic constitutive laws. *Computer Methods in Applied Mechanics and Engineering*, 381:113852, 2021.
- Ari L Frankel, Reese E Jones, and Laura P Swiler. Tensor basis gaussian process models of hyperelastic materials. *Journal of Machine Learning for Modeling and Computing*, 1(1), 2020.
- Alan D Freed, Daniel R Einstein, and Michael S Sacks. Hypoelastic soft tissues: part ii: in-plane biaxial experiments. *Acta mechanica*, 213(1-2):205–222, 2010.
- Jan N Fuhg and Nikolaos Bouklas. On physics-informed data-driven isotropic and anisotropic constitutive models through probabilistic machine learning and space-filling sampling. *Computer Methods in Applied Mechanics and Engineering*, 394:114915, 2022.
- David González, Alberto García-González, Francisco Chinesta, and Elías Cueto. A data-driven learning method for constitutive modeling: application to vascular hyperelastic soft tissues. *Materials*, 13(10):2319, 2020.
- Ian Goodfellow, Yoshua Bengio, and Aaron Courville. *Deep learning*. MIT press, 2016.
- Albert Edward Green. Hypo-elasticity and plasticity. ii. *Journal of Rational Mechanics and Analysis*, 5(5):725–734, 1956.
- Eitan Grinspun, Anil N Hirani, Mathieu Desbrun, and Peter Schröder. Discrete shells. In *Proceedings of the 2003 ACM SIGGRAPH/Eurographics symposium on Computer animation*, pages 62–67. Citeseer, 2003.
- Morton E Gurtin. *An introduction to continuum mechanics*. Academic press, 1982.
- Stefan Hartmann and Patrizio Neff. Polyconvexity of generalized polynomial-type hyperelastic strain energy functions for near-incompressibility. *International journal of solids and structures*, 40(11):2767–2791, 2003.
- Xiaolong He, Qizhi He, and Jiun-Shyan Chen. Deep autoencoders for physics-constrained data-driven nonlinear materials modeling. *Computer Methods in Applied Mechanics and Engineering*, 385:114034, 2021.
- Yousef Heider, Kun Wang, and WaiChing Sun. So (3)-invariance of informed-graph-based deep neural network for anisotropic elastoplastic materials. *Computer Methods in Applied Mechanics and Engineering*,

- 363:112875, 2020.
- R Hill. On uniqueness and stability in the theory of finite elastic strain. *Journal of the Mechanics and Physics of Solids*, 5(4):229–241, 1957.
- Gerhard A Holzapfel. *Nonlinear solid mechanics: a continuum approach for engineering science*, 2002.
- Gerhard A Holzapfel, Thomas C Gasser, and Ray W Ogden. A new constitutive framework for arterial wall mechanics and a comparative study of material models. *Journal of elasticity and the physical science of solids*, 61:1–48, 2000.
- Kurt Hornik, Maxwell Stinchcombe, and Halbert White. Multilayer feedforward networks are universal approximators. *Neural networks*, 2(5):359–366, 1989.
- Daniel Hsu, Clayton H Sanford, Rocco Servedio, and Emmanouil Vasileios Vlatakis-Gkaragkounis. On the approximation power of two-layer networks of random relus. In *Conference on Learning Theory*, pages 2423–2461. PMLR, 2021.
- Rubén Ibanez, Emmanuelle Abisset-Chavanne, Jose Vicente Aguado, David Gonzalez, Elias Cueto, and Francisco Chinesta. A manifold learning approach to data-driven computational elasticity and inelasticity. *Archives of Computational Methods in Engineering*, 25:47–57, 2018.
- Ilknur Icke and Joshua C Bongard. Improving genetic programming based symbolic regression using deterministic machine learning. In *2013 IEEE Congress on Evolutionary Computation*, pages 1763–1770. IEEE, 2013.
- Chi Jin, Sham M Kakade, and Praneeth Netrapalli. Provable efficient online matrix completion via non-convex stochastic gradient descent. *Advances in Neural Information Processing Systems*, 29, 2016.
- Karl A Kalina, Lennart Linden, Jörg Brummund, and Markus Kästner. Fe ann: an efficient data-driven multiscale approach based on physics-constrained neural networks and automated data mining. *Computational Mechanics*, 71(5):827–851, 2023.
- H Khajehsaeid, J Arghavani, and R30311651347 Naghdabadi. A hyperelastic constitutive model for rubber-like materials. *European Journal of Mechanics-A/Solids*, 38:144–151, 2013.
- Samuel Kim, Peter Y Lu, Srijon Mukherjee, Michael Gilbert, Li Jing, Vladimir Čeperić, and Marin Soljačić. Integration of neural network-based symbolic regression in deep learning for scientific discovery. *IEEE transactions on neural networks and learning systems*, 32(9):4166–4177, 2020.
- Diederik P Kingma and Jimmy Ba. Adam: A method for stochastic optimization. *arXiv preprint arXiv:1412.6980*, 2014.
- Trenton Kirchdoerfer and Michael Ortiz. Data-driven computational mechanics. *Computer Methods in Applied Mechanics and Engineering*, 304:81–101, 2016.
- Dominik K Klein, Mauricio Fernández, Robert J Martin, Patrizio Neff, and Oliver Weeger. Polyconvex anisotropic hyperelasticity with neural networks. *Journal of the Mechanics and Physics of Solids*, 159:104703, 2022.
- John R Koza. Genetic programming as a means for programming computers by natural selection. *Statistics and computing*, 4:87–112, 1994.
- Ellen Kuhl, Harm Askes, and Paul Steinmann. An illustration of the equivalence of the loss of ellipticity conditions in spatial and material settings of hyperelasticity. *European Journal of Mechanics-A/Solids*, 25(2):199–214, 2006.
- Isaac E Lagaris, Aristidis Likas, and Dimitrios I Fotiadis. Artificial neural networks for solving ordinary and partial differential equations. *IEEE transactions on neural networks*, 9(5):987–1000, 1998.
- Mikel Landajuela, Brenden K Petersen, Sookyung Kim, Claudio P Santiago, Ruben Glatt, Nathan Mundhenk, Jacob F Pettit, and Daniel Faissol. Discovering symbolic policies with deep reinforcement learning. In *International Conference on Machine Learning*, pages 5979–5989. PMLR, 2021.
- BA Le, Julien Yvonnet, and Q-C He. Computational homogenization of nonlinear elastic materials using neural networks. *International Journal for Numerical Methods in Engineering*, 104(12):1061–1084, 2015.
- Yves Le Guennec, J-P Brunet, F-Z Daim, Ming Chau, and Yves Tourbier. A parametric and non-intrusive reduced order model of car crash simulation. *Computer Methods in Applied Mechanics and Engineering*, 338:186–207, 2018.
- Guanghui Liang and K Chandrashekhara. Neural network based constitutive model for elastomeric foams. *Engineering structures*, 30(7):2002–2011, 2008.
- Kevin Linka and Ellen Kuhl. A new family of constitutive artificial neural networks towards automated model discovery. *Computer Methods in Applied Mechanics and Engineering*, 403:115731, 2023.

- Kevin Linka, Markus Hillgärtner, Kian P Abdolazizi, Roland C Aydin, Mikhail Itskov, and Christian J Cyron. Constitutive artificial neural networks: A fast and general approach to predictive data-driven constitutive modeling by deep learning. *Journal of Computational Physics*, 429:110010, 2021.
- Minliang Liu, Liang Liang, and Wei Sun. A generic physics-informed neural network-based constitutive model for soft biological tissues. *Computer methods in applied mechanics and engineering*, 372:113402, 2020.
- Jerrold E Marsden and Thomas JR Hughes. *Mathematical foundations of elasticity*. Courier Corporation, 1994.
- Filippo Masi, Ioannis Stefanou, Paolo Vannucci, and Victor Maffi-Berthier. Thermodynamics-based artificial neural networks for constitutive modeling. *Journal of the Mechanics and Physics of Solids*, 147:104277, 2021.
- L Angela Mihai, Silvia Budday, Gerhard A Holzapfel, Ellen Kuhl, and Alain Goriely. A family of hyperelastic models for human brain tissue. *Journal of the Mechanics and Physics of Solids*, 106:60–79, 2017.
- Melvin Mooney. A theory of large elastic deformation. *Journal of applied physics*, 11(9):582–592, 1940.
- Sonsoles Moreno, Víctor Jesús Amores, José Ma Benítez, and Francisco J Montáns. Reverse-engineering and modeling the 3d passive and active responses of skeletal muscle using a data-driven, non-parametric, spline-based procedure. *Journal of the Mechanical Behavior of Biomedical Materials*, 110:103877, 2020.
- Charles B Morrey Jr. Quasi-convexity and the lower semicontinuity of multiple integrals. 1952.
- Lu Trong Khiem Nguyen and Marc-André Keip. A data-driven approach to nonlinear elasticity. *Computers & Structures*, 194:97–115, 2018.
- Raymond W Ogden. *Non-linear elastic deformations*. Courier Corporation, 1997.
- Seong Joon Oh, Bernt Schiele, and Mario Fritz. Towards reverse-engineering black-box neural networks. *Explainable AI: Interpreting, Explaining and Visualizing Deep Learning*, pages 121–144, 2019.
- Hyungbum Park and Maenghyo Cho. Multiscale constitutive model using data-driven yield function. *Composites Part B: Engineering*, 216:108831, 2021.
- Adam Paszke, Sam Gross, Francisco Massa, Adam Lerer, James Bradbury, Gregory Chanan, Trevor Killeen, Zeming Lin, Natalia Gimelshein, Luca Antiga, et al. Pytorch: An imperative style, high-performance deep learning library. *Advances in neural information processing systems*, 32, 2019.
- Fabian Pedregosa, Gaël Varoquaux, Alexandre Gramfort, Vincent Michel, Bertrand Thirion, Olivier Grisel, Mathieu Blondel, Peter Prettenhofer, Ron Weiss, Vincent Dubourg, et al. Scikit-learn: Machine learning in python. *the Journal of machine Learning research*, 12:2825–2830, 2011.
- Brenden K Petersen, Mikel Landajuela, T Nathan Mundhenk, Claudio P Santiago, Soo K Kim, and Joanne T Kim. Deep symbolic regression: Recovering mathematical expressions from data via risk-seeking policy gradients. *arXiv preprint arXiv:1912.04871*, 2019.
- Auriane Platzer, Adrien Leygue, Laurent Stainier, and Michael Ortiz. Finite element solver for data-driven finite strain elasticity. *Computer Methods in Applied Mechanics and Engineering*, 379:113756, 2021.
- Maziar Raissi, Paris Perdikaris, and George E Karniadakis. Physics-informed neural networks: A deep learning framework for solving forward and inverse problems involving nonlinear partial differential equations. *Journal of Computational physics*, 378:686–707, 2019.
- Ronald S Rivlin and DW0042 Saunders. Large elastic deformations of isotropic materials vii. experiments on the deformation of rubber. *Philosophical Transactions of the Royal Society of London. Series A, Mathematical and Physical Sciences*, 243(865):251–288, 1951.
- Jörg Schröder and Patrizio Neff. Invariant formulation of hyperelastic transverse isotropy based on polyconvex free energy functions. *International journal of solids and structures*, 40(2):401–445, 2003.
- Jörg Schröder, Nils Viebahn, Peter Wriggers, Ferdinando Auricchio, and Karl Steeger. On the stability analysis of hyperelastic boundary value problems using three-and two-field mixed finite element formulations. *Computational Mechanics*, 60:479–492, 2017.
- Yuelin Shen, K Chandrashekhara, WF Breig, and LR Oliver. Neural network based constitutive model for rubber material. *Rubber chemistry and technology*, 77(2):257–277, 2004.
- M Shirani and DJ Steigmann. Convexity and quasiconvexity in a cosserat model for fiber-reinforced elastic solids. *Journal of Elasticity*, pages 1–13, 2022.
- Vahidullah Tac, Francisco Sahli Costabal, and Adrian B Tepole. Data-driven tissue mechanics with polyconvex neural ordinary differential equations. *Computer Methods in Applied Mechanics and Engineering*, 398:115248, 2022.
- Gregory H Teichert, Anirudh R Natarajan, Anton Van der Ven, and Krishna Garikipati. Machine learning materials physics: Integrable deep neural networks enable scale bridging by learning free energy

- functions. *Computer Methods in Applied Mechanics and Engineering*, 353:201–216, 2019.
- Prakash Thakolkaran, Akshay Joshi, Yiwen Zheng, Moritz Flaschel, Laura De Lorenzis, and Siddhant Kumar. Nn-euclid: Deep-learning hyperelasticity without stress data. *Journal of the Mechanics and Physics of Solids*, 169:105076, 2022.
- Leslie RG Treloar. Stress-strain data for vulcanized rubber under various types of deformation. *Rubber Chemistry and Technology*, 17(4):813–825, 1944.
- Clifford Truesdell. Hypo-elasticity. *Journal of Rational Mechanics and Analysis*, 4:83–1020, 1955.
- Clifford Truesdell, Walter Noll, C Truesdell, and W Noll. *The non-linear field theories of mechanics*. Springer, 2004.
- Clifford A Truesdell. *A First Course in Rational Continuum Mechanics V1*. Academic Press, 1992.
- Daniele Versino, Alberto Tonda, and Curt A Bronkhorst. Data driven modeling of plastic deformation. *Computer Methods in Applied Mechanics and Engineering*, 318:981–1004, 2017.
- Nikolaos N Vlassis and WaiChing Sun. Sobolev training of thermodynamic-informed neural networks for interpretable elasto-plasticity models with level set hardening. *Computer Methods in Applied Mechanics and Engineering*, 377:113695, 2021.
- Nikolaos N Vlassis, Ran Ma, and WaiChing Sun. Geometric deep learning for computational mechanics part i: Anisotropic hyperelasticity. *Computer Methods in Applied Mechanics and Engineering*, 371:113299, 2020.
- Nikolaos N Vlassis, Puhao Zhao, Ran Ma, Tommy Sewell, and WaiChing Sun. Molecular dynamics inferred transfer learning models for finite-strain hyperelasticity of monoclinic crystals: Sobolev training and validations against physical constraints. *International Journal for Numerical Methods in Engineering*, 123(17):3922–3949, 2022.
- Mingchuan Wang, Cai Chen, and Weijie Liu. Establish algebraic data-driven constitutive models for elastic solids with a tensorial sparse symbolic regression method and a hybrid feature selection technique. *Journal of the Mechanics and Physics of Solids*, 159:104742, 2022.
- Yiqun Wang, Nicholas Wagner, and James M Rondinelli. Symbolic regression in materials science. *MRS Communications*, 9(3):793–805, 2019.
- Zhenlin Wang, Jonathan B Estrada, Ellen M Arruda, and Krishna Garikipati. Inference of deformation mechanisms and constitutive response of soft material surrogates of biological tissue by full-field characterization and data-driven variational system identification. *Journal of the Mechanics and Physics of Solids*, 153:104474, 2021.
- Jeffrey A Weiss, Bradley N Maker, and Sanjay Govindjee. Finite element implementation of incompressible, transversely isotropic hyperelasticity. *Computer methods in applied mechanics and engineering*, 135(1-2):107–128, 1996.
- Kailai Xu, Daniel Z Huang, and Eric Darve. Learning constitutive relations using symmetric positive definite neural networks. *Journal of Computational Physics*, 428:110072, 2021.
- Tianhe Yu, Saurabh Kumar, Abhishek Gupta, Sergey Levine, Karol Hausman, and Chelsea Finn. Gradient surgery for multi-task learning. *Advances in Neural Information Processing Systems*, 33:5824–5836, 2020.